Development and experimental study of a small-scale compressed air radial inflow turbine for distributed power generation

Rahbar, Kiyarash; Mahmoud, Saad; Al-dadah, Raya K.; Moazami, Nima; Mirhadizadeh, Seyed A.

DOI:
10.1016/j.applthermaleng.2017.01.100

Document Version
Peer reviewed version

Citation for published version (Harvard):
Rahbar, K, Mahmoud, S, Al-dadah, RK, Moazami, N & Mirhadizadeh, SA 2017, 'Development and experimental study of a small-scale compressed air radial inflow turbine for distributed power generation', *Applied Thermal Engineering*, vol. 116, pp. 549-583. https://doi.org/10.1016/j.applthermaleng.2017.01.100

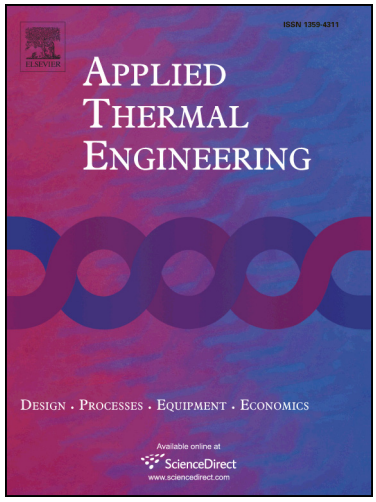

Development and Experimental Study of a Small-Scale Compressed Air Radial inflow Turbine for Distributed Power Generation

Kiyarash Rahbar, Saad Mahmoud, Raya K. Al-Dadah, Nima Moazami, Seyed A. Mirhadizadeh

PII: S1359-4311(16)32159-7
DOI: http://dx.doi.org/10.1016/j.applthermaleng.2017.01.100
Reference: ATE 9864

To appear in: *Applied Thermal Engineering*

Received Date: 4 October 2016
Revised Date: 16 January 2017
Accepted Date: 25 January 2017

Please cite this article as: K. Rahbar, S. Mahmoud, R.K. Al-Dadah, N. Moazami, S.A. Mirhadizadeh, Development and Experimental Study of a Small-Scale Compressed Air Radial inflow Turbine for Distributed Power Generation, *Applied Thermal Engineering* (2017), doi: http://dx.doi.org/10.1016/j.applthermaleng.2017.01.100

Development and Experimental Study of a Small-Scale Compressed Air Radial inflow Turbine for Distributed Power Generation

Kiyarash Rahbar[a*], Saad Mahmoud[a], Raya K. Al-Dadah[a], Nima Moazami[a], Seyed A. Mirhadizadeh[b]

[a] School of Mechanical Engineering, University of Birmingham, Edgbaston, Birmingham, B15 2TT, UK
[b] Johnson Matthey battery systems Ltd. Precedent house, Rooksley, Milton Keynes, MK13 8HF, UK

ABSTRACT

With ever increasing demand on energy, disturbed power generation utilizing efficient technologies such as compressed air energy storage (CAES) or organic Rankine cycle (ORC) are receiving growing attention. Expander for such systems is a key component and its performance has substantial effects on overall system efficiency. This study addresses such component by proposing an effective and comprehensive methodology for developing a small-scale radial inflow turbine (RIT). The methodology consists of 1-D modelling, 3-D aerodynamic investigation and structural analysis, manufacturing with pioneering technique and experimental testing for validation. The proposed 1-D modelling was very effective in determining the primary geometry and performance of turbine based on parametric studies of turbine input design variables. However with CFD analysis, it was shown that more efficient turbine geometry can be achieved that not only provides more realistic turbine performance by capturing the 3-D fluid flow behaviour but also improves turbine efficiency with the aid of parametric studies of turbine geometry parameters. Turbine efficiency was improved from 81.3% obtained from 1-D modelling to 84.5% obtained by CFD. Accuracy of the CFD model was assessed by conducting experiments on the RIT manufactured with stereolithography technique. The CFD model can predict turbine efficiency and power with accuracy of ±16% and ±13% respectively for a wide range of tested operating conditions. Such results highlights the effectiveness of the proposed methodology and the CFD model can be used as benchmarking model for analyses of small-scale RITs. Besides, it was shown that for such applications, the novel manufacturing technique and employed material are very effective for producing prototypes that assist design decisions and validation of CFD model with reasonable accuracy at reasonable cost and in timely manner.

Keywords: Radial turbine; Distributed power generation; CFD; Experimental; Additive layer manufacturing (3D printing); Stereolithography

[*]Corresponding author. Tel.: +44(0)1214143513; fax: +44(0)1214143958. E-mail addresses: kiyarash.rahbar@gmail.com , kxr965@alumni.bham.ac.uk

1. Introduction

Nowadays energy is a key factor in the global economy and the effectiveness of energy generation and consumption processes has remarkable impacts on our society and environment. Following the international energy agency (IEA) report [1], extending the current trend of energy consumption and energy efficiency to 2050 yields a growth of 70% and 60% in the global energy demands and emissions respectively compared to 2011. The associated emissions result in a long-term global average temperature rise of 6°C by 2050 which can result in potentially devastating consequences such as climate change and energy security. IEA (2014) suggested an effective scenario called "2DS" which offers a vision for a sustainable energy system that reduces CO_2 emissions to maintain the global temperature rise within 2°C by 2050 and to limit increases in energy demand by 25% and cut emissions by 50%. This strategy creates a framework for a future sustainable energy systems which are expected to be smarter, renewable oriented, integrated, well-regulated and more distributed.

Improvements in energy efficiency have significant contribution to the "2DS" scenario. For example, power in the traditional electrical grid (or centralized power generation) followed one way from the generation station to the load. The traditional grid uses the highest possible voltage level transmit and distribute power with associated losses of about 12% of power and 30% of delivered electricity cost [2]. In addition, there are implicit costs in terms of carbon emissions in which the fuel that is consumed to generate electricity is not fully consumed by the end user. Moreover, centralized power generation (CPG) requires large capital investment cost for electrification of remote areas where the infrastructure requires the electricity but at low quantities. CPG suffers from high cost of electricity deregulation and control devices and harmful environmental impacts due to the use of fossil fuels. Therefore, it is necessary to minimize these losses in order to increase the energy efficiency.

In this regard, distributed (on-site) power generation (DPG) is a promising alternative that overcomes all the deficiencies of the CPG. DPG is an independent electric source connected directly to the distribution network or to the customer site with power ratings shown in Table 1 [3].

Table 1 Power rating of DPG systems [3]

Category	Power rating
Distributed micro power generation	1Watt to 5KW
Distributed small power generation	5KW to 5MW
Distributed medium power generation	5MW to 50MW
Distributed large power generation	50MW to 300MW

DPG is becoming a new trend in the world's ever-increasing demand for energy as it exhibits unique advantages such as reduced transmission and distribution losses, emergency backup power in the case of power outage for hospitals, telecommunications centres and data storage centres, lower damages and economic losses in case of natural disasters, environmentally friendlier than CPG and versatility for supplying electricity demand in remote areas.

Compressed air energy storage (CAES) is a cost effective technology that can be used for DPG systems where the surplus of electrical energy is stored in the form of high-pressure air in underground or aboveground storage reservoirs by running a compressor. Then during peak demand compressed air is released and expanded through an expander to generate electricity [4]. Compare to the Brayton cycle, CAES can save up to two-third of the generated electricity by storing air and recovering it later [5]. This is due to the fact that expander's output no longer needs to be used to drive the air compressor [6]. Therefore, developing an efficient expander is vital for CAES application and can play an important role in increasing the efficiency of this energy conversion process for DPG systems. Briola *et al*. [7] proposed a mathematical model for assessment of adiabatic CAES. The model consists characteristic curve of the turbomachinery equipment (compressor and turbine). Results showed that turbine and compressor characteristic curves are required to be identified in such a way that operation points of turbomachinery lay within admissible range during the entire process. The developed model was only capable of determining some geometry parameters of turbine with known dimensionless velocity. Zhao *et al.* [8] executed the analysis of energy efficiency of CAES with constant volume using an axial turbine as the expander under two pressure modes as constant and variable at turbine inlet. They used heat rate, energy generated per unit volume of storage and second law efficiency to evaluate the energy losses of each components of CAES system under different operation modes. Heat rate was defined as the ratio between the input fuel energy and the total work output while energy generated per unit volume of storage was defined as the ratio between the total work output and the air

storage size. At design point operating condition, the former mode's second law efficiency was 44.56% while for the latter it was shown to be 45.16%. At the off-design both load rate and speed levels have positive effect on exergy efficiency and the energy generated per unit volume of storage, but have negative effect on heat rate. Maia *et al.* [9] conducted experimental evaluation of a micro-CAES system while adopting an automotive turbocharger turbine as expander. The turbine showed maximum power output of 3.5 kWe at 70,000 RPM with efficiency of 76% while maximum system efficiency was about 45% when operating with air at ambient temperatures without external sources of heat. Ennil *et al.* [10] proposed a methodology for minimization of losses in small-scale air-driven axial turbine suitable for CAES systems. The proposed method was based on fully automated CFD simulation coupled with Multi-objective genetic algorithm (MOGA) technique. Results showed that the Kacker & Okapuu model predicted the closest values to CFD simulation which can be further maximized through CFD optimization with maximum improvement of 12.5%. Yao *et al.* [11] proposed a combined heat and power (CHP) system based on small-scale CAES. Sensitivity analyses results showed that inlet pressure and temperature of turbine, and effectiveness of heat exchangers have dominant influence on the system performance. Additionally, it was shown by multi-objective optimization that, trade-off between the thermodynamic and economic performances was necessary to achieve the maximum exergy efficiency of 52.51% in a cost-effective way.

Organic Rankine cycle (ORC) is another efficient technology supplying electricity demand through the DPG system by converting almost any kind of low to medium grade heat into useful power while utilizing working fluids that boil at low temperature and pressure. Expander is the critical component in a relatively efficient ORC system and has significant effect on the overall cycle performance [12]. Martines *et al.* [13] analysed the application of a single stage partial admission axial turbine for the ORC. Turbine geometry was optimized to achieve maximum efficiency under several subcritical and supercritical cycle conditions. Turbine preliminary design was shown to be greatly influenced by media compressibility and use of convergent-divergent profiled nozzles was shown promising to achieve the highest performance at elevated evaporator pressure. Manente *et al.* [14] investigated the effect of an axial turbine performance maps on ORC performance both under subcritical and supercritical operating conditions. The model included an optimization algorithm to maximize turbine efficiency. Results showed that supercritical ORCs outperformed subcritical ORCs by an average value of 20% even taking into account the detrimental effect of high expansion ratios

on turbine efficiency. Rahbar *et al.* [15-18] proposed an integrated modelling technique that combined the mean-line modelling of radial inflow turbine (RIT) with ORC and coupled with genetic algorithm that allowed multi-objective optimization of turbine isentropic efficiency and cycle thermal efficiency based on a wide range of input parameters. They showed that with such technique it is possible to obtain significantly higher performance by comparing their results with the literature.

Among available expanders, RIT exhibits unique advantages of high isentropic efficiency, high power capacity, small number of moving parts, mature manufacturability and high power to weight ratio and is particularly attractive for small-scale units. Table 2 outlines comparison of available expanders that can be used with CAES or ORC systems.

This study proposed an effective and comprehensive methodology for developing small-scale RIT as the expander of CAES or ORC systems. This method encompasses 1-D modelling, 3-D aerodynamic investigation using CFD, 3-D finite element analysis for assessing mechanical integrity, 3-D solid modelling, fabricating with pioneering material and manufacturing technique and experimental testing for validation of modelling and simulation approaches. For this study specifically, the proposed methodology will be employed for developing a small-scale RIT for CAES application with the power capacity of up to 5kW (distributed micro power generation). Potential and effectiveness of such methodology for improving turbine performance will be highlighted and can be served as basis for other applications.

Table 2 Comparison of various expanders

Type	Advantages	Drawbacks
Scroll expander	1. Light weight 2. Low rotational speed 3. No inlet and exhaust valves which reduce noise	1. Low power capacity 2. Significant lubrication to operate without wear 3. Most kinetically complex geometry compared to other volumetric expanders 4. Under and over expansion losses if there is mismatch between ORC and expander nominal volume ratios 5. Friction, suction and internal leakage losses
Screw expander	1. Tolerate two-phase flow 2. Low rotational speed	1. Lubrication requirement 2. Difficult manufacturing with tight tolerances 3. Critical sealing requirements 4. High cost 5. Limited internal built-in volume ratio due to length of rotor
Reciprocating piston expander	1. Higher pressure ratio compared to other volumetric expanders 3. Mature manufacturability	1. Large number of moving parts with high friction and wearing 2. Heavy weight 3. Torque impulse 4. Requires precise timing for inlet and exhaust valves 5. Critical balancing requirements

Radial inflow turbine	1. High efficiency 2. Light weight 3. Compact layout 4. Mature manufacturability 5. High power to weight ratio 6. Small number of moving parts 7. Stability	1. High rotational speed
Axial flow turbine	1. Suitable for high power capacity (more than 50kWe) and large flow rates 2. High efficiency at large power capacity	1. High blade profile accuracy required at high cost 2. High axial force and thrust bearing losses 3. Expensive manufacturing process (blades and disk)

2. Radial inflow turbine (RIT) architecture

The RIT consists of four key components as volute (casing), nozzle, rotor and diffuser as illustrated in Figure 1. The incoming fluid is accelerated and distributed around the periphery of the turbine via volute (1-2). Further acceleration and increase in tangential component of velocity is achieved by nozzle ring (2-3) before it enters the rotor. The empty space between the nozzle and rotor (3-4) allows for the nozzle outlet wakes to mix out [19]. Then the kinetic energy of the fluid is converted into mechanical energy of shaft as it expands through the rotor (4-5). If the kinetic energy of exhaust is significant, with specific speed (N_s) as high as 0.7, a diffuser can be employed to recover the otherwise wasted energy (5-6). N_s is a non-dimensional parameter that allows choice of the most appropriate machine based on actual performance correlation charts as well as describing turbine operating requirements in terms of shaft speed, volume flow rate and ideal specific work [19]. The corresponding enthalpy-entropy diagram detailing expansion process across the stage is shown in Figure 1.

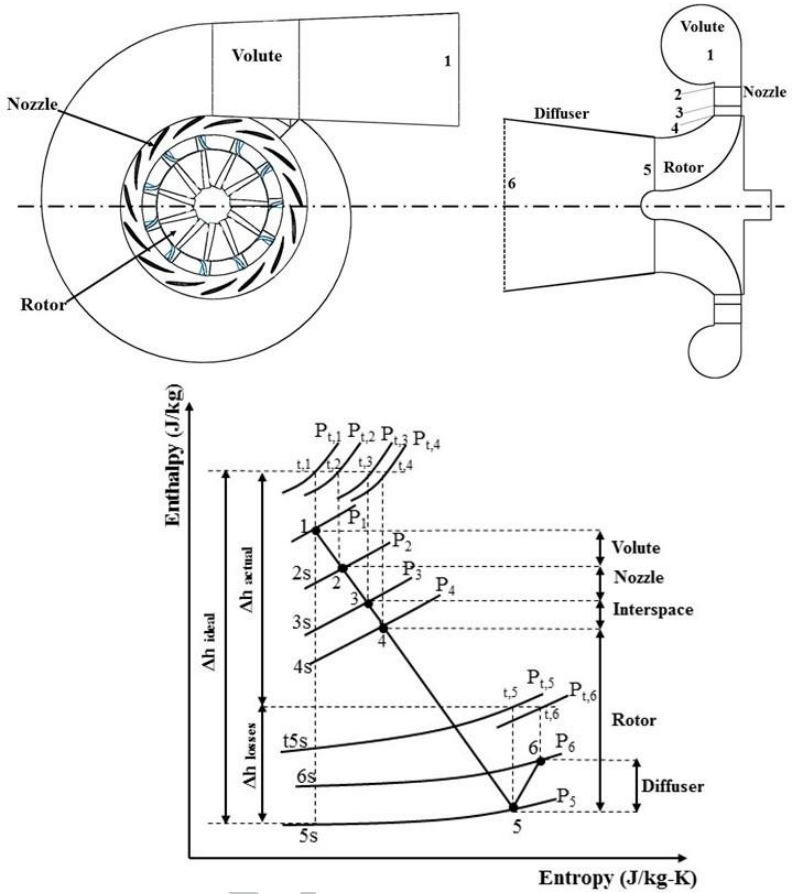

Figure 1 Schematic of radial inflow turbine components, (top left) front view, (top right) meridional view, (bottom) enthalpy-entropy diagram of turbine stage expansion

3. Overview of development methodology of RIT

Figure 2 outlines overview of the proposed methodology for development of RIT. Initial stage is the mean-line (one-dimensional) modelling. Mean-line modelling determines the overall geometrical parameters of the RIT at a set of key stations (Figure 1) together with an estimate of the turbine performance based on the specified input parameters. Since the mean-line modelling involves exploration of a very large design space, it is required to conduct systematic parametric study to investigate the effect of turbine design parameters on its performance [20]. Then for the candidate design suggested by the mean-line modelling, full 3-D blade geometry is defined using the key geometry parameters transferred from the mean-line to a computer aided design (CAD) package. Although it is fast, the simple 1-D (mean-line) model cannot thoroughly capture the complex behaviour of the RIT as the flow is strongly 3-D, viscous and turbulent. Hence, it is required to evaluate aerodynamics of the created blade geometry in more details using viscous (RANS equations) CFD simulations and if necessary modify geometry to improve the performance. Simultaneously, it is necessary to

evaluate mechanical integrity of the 3-D blades using finite element analysis (FEA) and assess the blade stress and displacement due to the fluid pressure and centrifugal forces. When the blade geometries (nozzle and rotor) are satisfactory, it is required to carry out solid modelling and drafting of the complete assembly together with the design and selection of complementary components such as shaft, bearings and seals. The complete assembly will be manufactured for laboratory testing and results will be validated with the experiments.

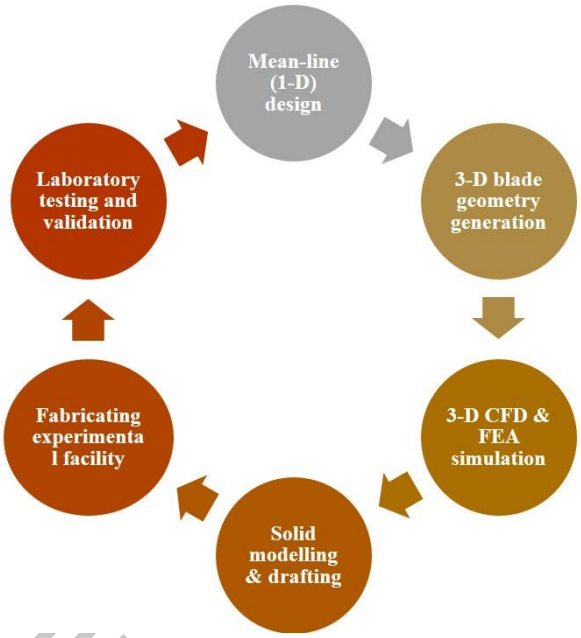

Figure 2 Overview of the methodology

3.1. Mean-line (one-dimensional) modelling and performance estimation

3.1.1. Overview of the mean-line procedure

Mean-line modelling is based on a one-dimensional assumption that the fluid's properties are constant on a plane normal to its direction of motion and thus vary only in one direction that follows the geometry of blades on the mean streamline and such line represents the average of the passage conditions [21]. Mean-line modelling determines the flow dynamic properties and geometric parameters at key stations throughout the stage. Mean-line modelling is a highly iterative process since it requires comprehensive studies of many different configurations by exploring a large design space created by variation of a large group of input parameters. Inputs to the mean-line model include the operating conditions (i.e. turbine inlet total temperature and pressure), non-dimensional parameters (i.e. velocity ratio) and geometry ratios (i.e. ratio of rotor exit hub to tip radii). With the provided inputs

and initial guess of turbine isentropic efficiency, the preliminary design of rotor is carried out. Based on this, overall characteristics for the remaining components are determined. Using these results and the loss correlations, the model determines a more accurate prediction of the turbine stage efficiency. This value is then used as the initial guess for the turbine efficiency and the process is repeated until convergence is achieved to the specified tolerance. Figure 3 outlines the flowchart of mean-line model detailing the overall procedure. The mean-line model is implemented into the engineering equation solver (EES) software [22]. This allows the use of its extensive and reliable built-in functions to determine thermodynamic properties.

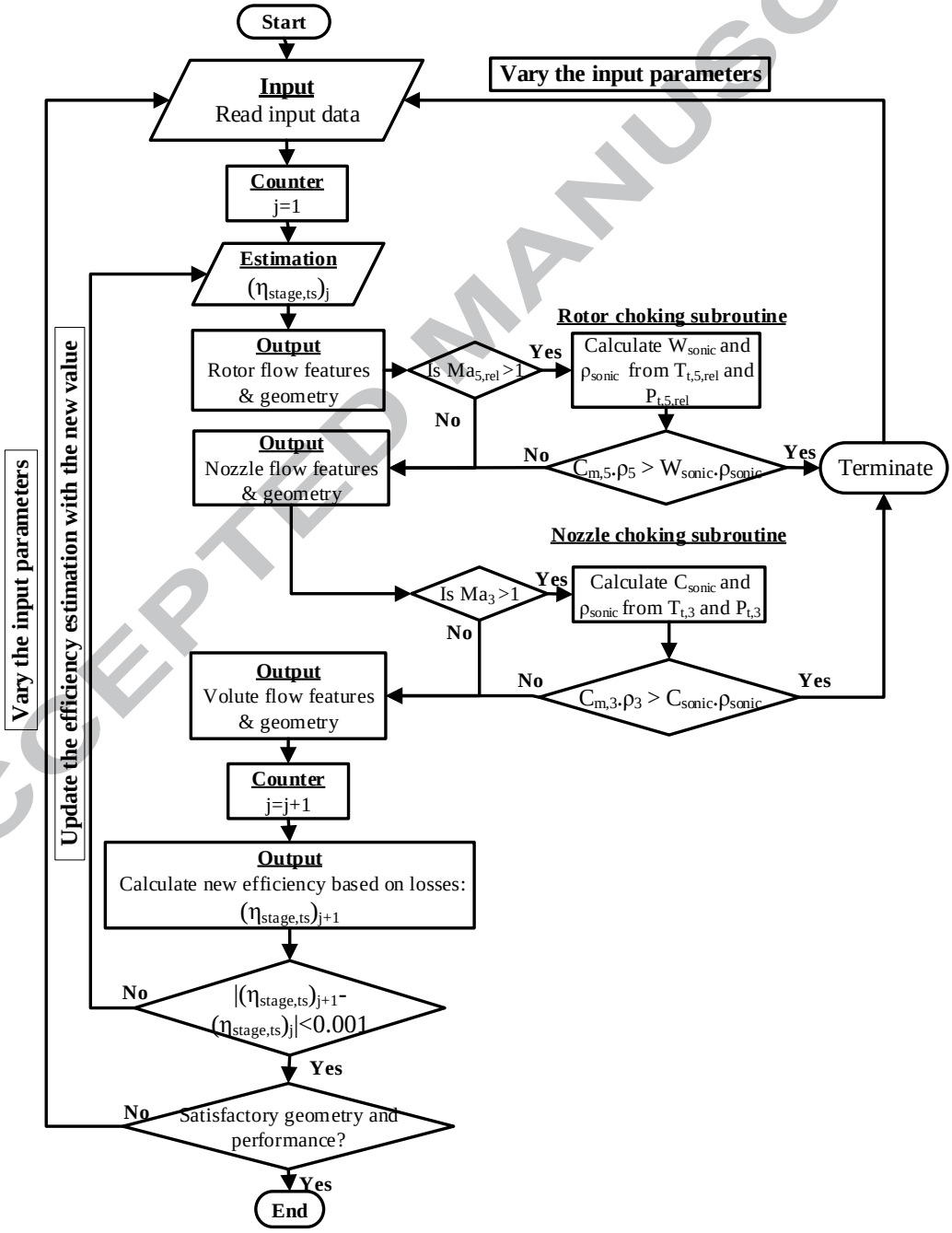

Figure 3 Flowchart of the mean-line model adopted from [16]

3.1.2. Rotor modelling

For rotor modelling velocity ratio (v), a non-dimensional design parameter, together with turbine inputs (Table 3) are employed to establish the rotor principal geometry and velocity triangles at inlet and exit as shown in Figure 4.

Table 3 Mean-line input parameters and their range

Parameter	Unit	Range
Operating parameters		
Inlet total temperature ($T_{t,1}$)	K	323 - 473
Inlet total pressure ($P_{t,1}$)	kPa	150 - 400
Expansion ratio (ER_{ts})	(-)	1.5 - 3
Mass flow rate ($\dot{m}$)	kg/s	0.03 - 0.1
Turbine design parameters		
Velocity ratio (v_{ts})	(-)	0.6 - 0.9
Rotational speed (ω)	rpm	40000 - 60000
Rotor inlet absolute flow angle (α_4)	degree	60 - 80
Rotor exit absolute flow angle (α_5)	degree	-10 - 10
Rotor exit hub to inlet radii ratio ($r_{5,hub}/r_4$)	(-)	0.15 - 0.45
Rotor exit tip to inlet radii ratio ($r_{5,tip}/r_4$)	(-)	0.5 - 0.8

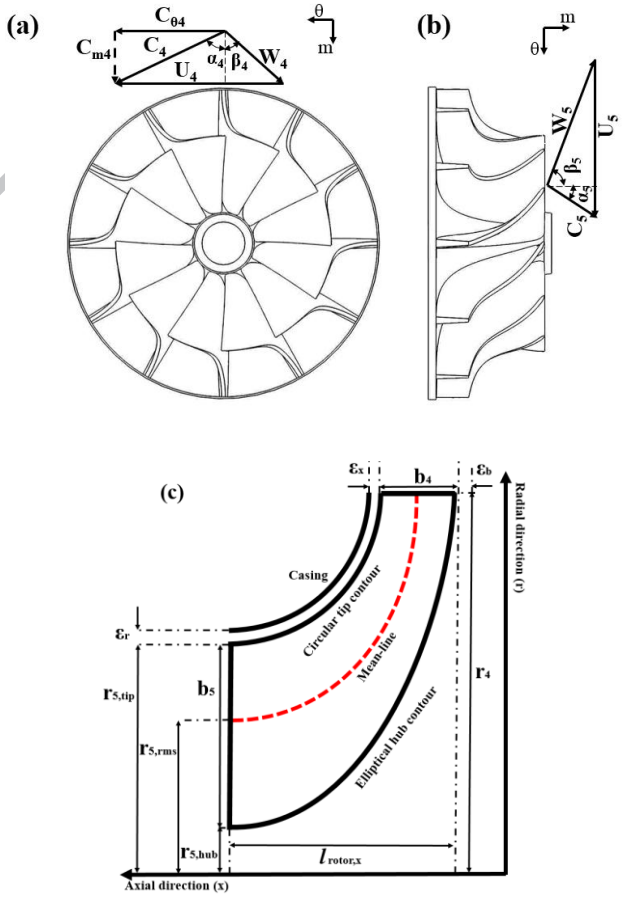

Figure 4 Rotor inlet and exit velocity triangles (a, b), meridional view of the turbine rotor with notion of principal dimensions (c)

The velocity ratio can be described with ideal-gas laws using Equation 1.

$$\nu = \frac{U_4}{C_s} = \frac{U_4}{\sqrt{2C_P T_{t,1}\left(1 - \left(\frac{P_5}{P_{t,1}}\right)^{\frac{\gamma-1}{\gamma}}\right)}} \quad \text{Equation 1}$$

Where C_s is the spouting velocity. With the known turbine input parameters (Table 3), C_s can be immediately calculated leading to determination of the rotor wheel inlet velocity (U_4) with the pre-set ν value. Consequently, the rotor inlet radius (r_4), actual specific enthalpy drop (Δh_{actual}) and power will be obtained as below:

$$r_4 = \frac{U_4}{\omega} \quad \text{Equation 2}$$

$$\Delta h_{actual} = 0.5 C_s^2 \eta_{stage,ts} \quad \text{Equation 3}$$

$$Power = \dot{m} \Delta h_{actual} \quad \text{Equation 4}$$

Where the stage total-to-static efficiency ($\eta_{stage,ts}$) will be iterated based on the loss models as will be discussed in the following sections.

With the known r_4 the rotor exit hub and tip radii ($r_{5,hub}$, $r_{5,tip}$) can be found with the input geometry ratios (Table 3) and consequently rotor exit flow area (A_5) and $r_{5,rms}$ are calculated accordingly.

$$A_5 = \pi(r_{5,tip}^2 - r_{5,hub}^2)(1 - \mathrm{BK}) \quad \text{Equation 5}$$

$$r_{5,rms} = \sqrt{\frac{A_5}{2\pi} + r_{5,hub}^2} \quad \text{Equation 6}$$

Where *BK* is the blockage factor due to the effect of boundary layer growth at the rotor exit with the value of 0.1 as suggested in [23]. With the adiabatic assumption ($T_{t,1} = T_{t,4}$), total thermodynamic properties at the rotor inlet and exit are obtained as following [19, 24]:

$$P_{t,4} = P_{t,1} - \left(\rho_{t,1} C_s^2 \frac{1 - \eta_{stage,ts}}{8}\right) = P_{t,1} - \left(\rho_{t,1} \Delta h_{actual} \frac{1 - \eta_{stage,ts}}{4\eta_{stage,ts}}\right) \quad \text{Equation 7}$$

$$T_{t,5} = T_{t,1}\left(1 - \eta_{stage,ts}\left(1 - \left(\frac{1}{ER_{ts}}\right)^{\frac{\gamma-1}{\gamma}}\right)\right) \quad \text{Equation 8}$$

Euler turbomachinery equation (Equation 9) was used for calculating the velocity triangles both at the inlet and outlet of rotor blades.

$$\Delta h_{actual} = U_4 C_{\theta,4} - U_5 C_{\theta,5} = \frac{1}{2}[(U_4^2 - U_5^2) - (W_4^2 - W_5^2) + (C_4^2 - C_5^2)] \quad \text{Equation 9}$$

As suggested in [19, 21, 24] the rotor exit swirl angle (α_5) is often considered to be zero in order to reduce the rotor exit kinetic loss and then Equation 9 can be readily solved for $C_{\theta,4}$. Subsequently, solution for the velocity triangles are obtained with the known rotor inlet absolute flow angle (α_4) (Table 3) and trigonometric rules. Static thermodynamic properties at the rotor inlet and exit as well as rotor inlet width (b_4) are obtained as following:

$$T_4 = T_{t,4} - \frac{C_4^2}{2C_p} \quad \text{Equation 10}$$

$$P_4 = P_{t,4}\left(\frac{T_4}{T_{t,4}}\right)^{\frac{\gamma}{\gamma-1}} \quad \text{Equation 11}$$

$$T_5 = T_{t,5} - \frac{C_5^2}{2C_p} \quad \text{Equation 12}$$

$$P_5 = P_{t,5}\left(\frac{T_5}{T_{t,5}}\right)^{\frac{\gamma}{\gamma-1}} \quad \text{Equation 13}$$

$$b_4 = \frac{\dot{m}RT_4}{2\pi r_4 C_{m,4} P_4} \quad \text{Equation 14}$$

The rotor axial length ($l_{rotor,x}$) and the number of rotor blades (Z_{rotor}) are determined from correlations in [24] and [25] respectively.

$$l_{rotor,x} = 1.5(r_{5,tip} - r_{5,hub}) \quad \text{Equation 15}$$

$$Z_{rotor} = \frac{\pi}{30}(110 - \alpha_4)\tan\alpha_4 \quad \text{Equation 16}$$

If none-zero exit swirl is to be adopted ($\alpha_5 \neq 0$), the solving algorithm shown in Figure 5 is implemented into the mean-line code following [20].

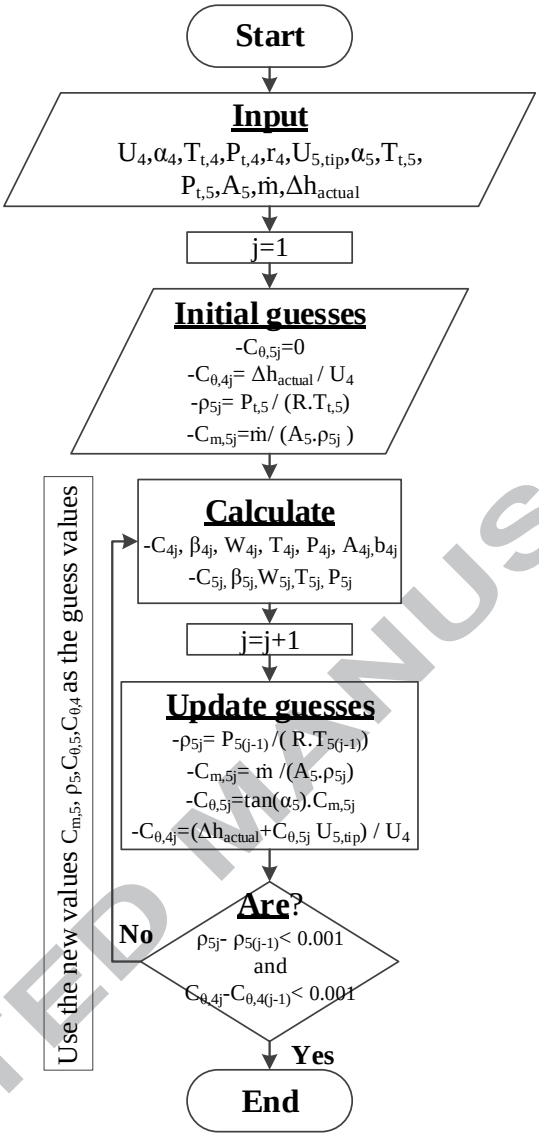

Figure 5 Algorithm for calculating velocity triangles and static thermodynamic properties for any value of α_5 (adopted form [20])

3.1.3. Nozzle modelling

For nozzle modelling a constant blade height equal to the rotor inlet blade height is assumed (b_3=b_4) along the length of nozzle vanes while the nozzle exit absolute flow angle is also set to be the same as the rotor inlet absolute flow angle (α_3= α_4) as shown in Figure 6. With the assumption of isentropic expansion in the casing and interspace [26], the thermodynamic properties and absolute velocities (C_2, C_3) both at inlet and exit are obtained iteratively using conservation of mass and angular momentum, thermodynamic properties ($P_{t,1}$, $T_{t,1}$, $Pt_{,4}$, $T_{t,4}$), Equations 17 [27] and 18.

$$r_3 = r_4 + 2b_4 \cos \alpha_4 \qquad \text{Equation 17}$$

$$C_{\theta,3} = \frac{C_{\theta,4} r_4}{r_3}$$ Equation 18

The nozzle inlet to exit radii ratio (r_2/r_3) and nozzle solidity (σ) are set to 1.25 and 1.35 respectively as suggested in [25]. Consequently the nozzle chord length (C_{nozzle}), nozzle pitch (S_{nozzle}) and number of nozzle blades (Z_{nozzle}) are determined as following:

$$C_{nozzle} = \sqrt{\left| r_2^2 + r_3^2 - \sqrt{\left| (r_2^2 + r_3^2)^2 - \left(\frac{r_2^2 + r_3^2}{\cos\left(\frac{\alpha_2 + \alpha_3}{2}\right)} \right)^2 \right|} \right|}$$ Equation 19

$$S_{nozzle} = \frac{C_{nozzle}}{\sigma}$$ Equation 20

$$Z_{nozzle} = \frac{2\pi r_3}{S_{nozzle}}$$ Equation 21

Accordingly, the nozzle throat opening (O_{throat}) and nozzle total throat area ($A_{throat,total}$) are determined ignoring the nozzle vanes trailing edge thickness for simplicity.

$$O_{throat} = S_{nozzle} \cos \alpha_3$$ Equation 22

$$A_{throat,total} = O_{throat} b_3 Z_{nozzle}$$ Equation 23

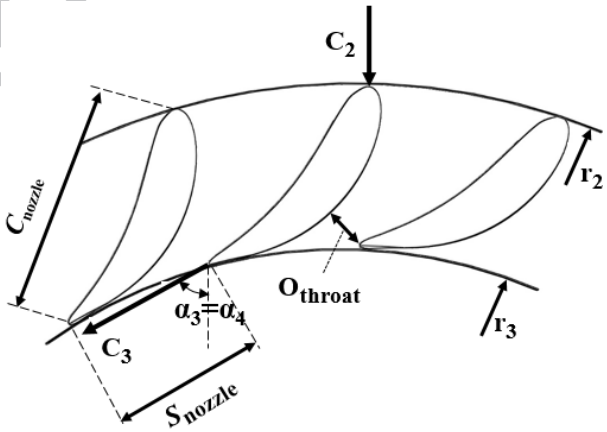

Figure 6 Schematic of nozzle ring with corresponding geometry and velocity vectors

3.1.4. Performance estimation with loss models

The turbine stage total-to-static isentropic efficiency is defined by Equation 24 where losses are considered as the difference between ideal and actual enthalpy drops as shown in Figure 1.

$$\eta_{stage,ts} = \frac{\Delta h_{actual}}{\Delta h_{ideal}} = \frac{\Delta h_{actual}}{\Delta h_{actual} + \sum \Delta h_{losses}} \quad \text{Equation 24}$$

3.1.4.1. Incidence loss

Incidence loss is the enthalpy drop due to flow disturbance at the rotor blade inlet when the rotor flow angle is different form the optimum angle (incidence angle) [28].

$$\Delta h_{incidence} = \frac{W_{\theta,4}^2}{2} \quad \text{Equation 25}$$

Where $W_{\theta,4}$ is relative tangential (circumferential) flow velocity at the rotor inlet.

3.1.4.2. Friction loss

The friction loss generated due to the shear forces between the flow and rotor blade's solid surface [28].

$$\Delta h_{friction} = f_{curve}\left(\frac{W_4 + \left(\frac{W_{5,tip} + W_{5,hub}}{2}\right)}{2}\right)^2 \frac{l_{hyd}}{d_{hyd}} \quad \text{Equation 26}$$

Where f_{curve} is the friction factor that is modified to account for curvature effects of RIT [29].

$$f_{curve} = f\left(1 + 0.075\overline{Re}^{0.25}\sqrt{\frac{d_{hyd}}{2r_c}}\right)\left(\overline{Re}\left(\frac{d_4}{2r_c}\right)^2\right)^{0.05} \quad \text{Equation 27}$$

Where f is the friction factor and obtained as below [30].

$$f = 8\left(\left(\frac{8}{\overline{Re}}\right)^{12} + \left(\left(2.457ln\left(\frac{1}{\left(\frac{7}{\overline{Re}}\right)^{0.9} + 0.27RR}\right)\right)^{16} + \left(\frac{37530}{\overline{Re}}\right)^{16}\right)^{-1.5}\right)^{\frac{1}{12}} \quad \text{Equation 28}$$

RR is the wall relative roughness with the value of 0.0002m suggested by [28]. $\overline{Re}$ is the averaged Reynolds number between the rotor inlet and exit.

$$\overline{Re} = \frac{\frac{U_4 b_4 \rho_4}{\mu_4} + \frac{U_5 b_6 \rho_5}{\mu_5}}{2} \quad \text{Equation 29}$$

The rotor hydraulic length (l_{hyd}) and hydraulic diameter (d_{hyd}) are obtained as following [19, 25].

$$l_{hyd} = \frac{\pi}{2}\left(\sqrt{\frac{\left(r_4 - r_{5,tip} + \frac{b_4}{2}\right)^2 + \left(\frac{b_5}{2}\right)^2}{2}}\right) \quad \text{Equation 30}$$

$$d_{hyd} = 0.5\left(\frac{4\pi r_4 b_4}{2\pi r_4 + Z_{rotor} b_4} + \frac{2\pi(r_{5,tip}^2 - r_{5,hub}^2)}{\pi(b_5) + Z_{rotor}(b_5)}\right) \quad \text{Equation 31}$$

The rotor mean radius of curvature (r_c) is calculated as below.

$$r_c = r_4 - r_{5,tip} + \frac{b_4 + b_5}{2} \quad \text{Equation 32}$$

3.1.4.3. Secondary loss

Local flow circulations imposed on the main flow (secondary flows) almost inevitably occur in the RIT due to the simultaneous radius change in the meridional plane and strong pressure gradient in the blade-to-blade plane [31].

$$\Delta h_{secondary} = \frac{C_4^2 d_4}{Z_{rotor} r_c} \quad \text{Equation 33}$$

3.1.4.4. Tip clearance loss

Due to the necessary running clearance between rotor tip and casing (Figure 4) some of the flow is leaked through the gap from the pressure to suction surface without utilizing its kinetic energy to create mechanical work [23].

$$\Delta h_{tip\ clearance} = \frac{U_4^3 Z_{rotor}}{8\pi}\left(0.4\varepsilon_x C_x + 0.75\varepsilon_r C_r - 0.3\sqrt{\varepsilon_x \varepsilon_r C_x C_r}\right) \quad \text{Equation 34}$$

$$C_x = \frac{1 - \left(\frac{r_{5,tip}}{r_4}\right)}{C_{m,4} b_4} \quad \text{Equation 35}$$

$$C_r = \left(\frac{r_{5,tip}}{r_4}\right)\frac{l_{rotor,x} - b_4}{C_{m,5} r_5 b_5} \quad \text{Equation 36}$$

Where ε_x and ε_r are the axial and radial tip clearances.

$$\varepsilon_x = \varepsilon_r = \varepsilon_b = 0.04(b_5) \quad \text{Equation 37}$$

3.1.4.5. Exit kinetic loss

Exit kinetic loss is the enthalpy drop due to the wasted kinetic energy of exhaust which has not been completely converted into the shaft mechanical work.

$$\Delta h_{exit} = \frac{C_5^2}{2} \qquad \text{Equation 38}$$

3.1.4.6. Windage loss

Windage (disc friction) loss is due to the fluid leakage between the back face of rotor disc and stationary turbine back plate [21].

$$\Delta h_{windage} = \frac{k_f \bar{\rho} U_4^3 r_4^2}{4\dot{m}} \qquad \text{Equation 39}$$

Where $\bar{\rho}$ is the average density between the rotor inlet and exit, ε_b is the rotor back plate clearance and obtained by Equation 37 [21].

$$k_f = 3.7 \frac{\left(\frac{\varepsilon_b}{r_4}\right)^{0.1}}{Re^{0.5}} \quad for\ Re < 10^5 \qquad \text{Equation 40 (a)}$$

$$k_f = 0.102 \frac{\left(\frac{\varepsilon_b}{r_4}\right)^{0.1}}{Re^{0.2}} \quad for\ Re > 10^5 \qquad \text{Equation 40 (b)}$$

3.1.4.7. Nozzle friction loss

Nozzle friction loss is found by Equation 41 [21] where $\bar{C}$ is the average of the nozzle inlet and exit absolute velocities and f is obtained by Equation 28.

$$\Delta h_{friction,nozzle} = 4 f \bar{C}^2 \frac{l_{hyd,nozzle}}{d_{hyd,nozzle}} \qquad \text{Equation 41}$$

$$l_{hyd,nozzle} = r_2 - r_3 \qquad \text{Equation 42}$$

$$d_{hyd,nozzle} = 0.5 \left(\frac{8\pi r_2 b_3 \cos\alpha_2}{4\pi r_2 + \frac{4\pi r_2 b_3}{\sigma}} + \frac{8\pi r_3 b_3 \cos\alpha_3}{4\pi r_3 + \frac{4\pi r_3 b_3}{\sigma}} \right) \qquad \text{Equation 43}$$

3.2. Overview of CFD and FEA simulations

The actual flow field in the RIT is strongly 3-D, viscous and turbulent with inevitable secondary flow regions. In addition, tip clearance effects and interactions of adjacent nozzle

and rotor blade rows make the flow behaviour even more complex. Although it is fast and simple, mean-line (one-dimensional) modelling cannot capture all the aforementioned features and it is required to evaluate the aerodynamics of the turbine passage in greater details using computational fluid dynamic (CFD). CFD facilitates the investigation of the flow in turbine passage accurately to directly address those undesirable features by improving the blade geometry. The key geometric characteristics of the candidate turbine stage obtained from mean-line modelling are used as input for 3-D geometry generation of the nozzle and rotor blades using ANSYS^{R15} BladeGen. Afterwards, grid will be created via structured hexagonal elements using ANSYS^{R15} TurboGrid. The selected boundary conditions from the mean-line modelling are used to perform CFD analysis using ANSYS^{R15} CFX. The obtained fluid pressure distribution across blade surface area together with blade rotational speed are used to conduct FEA with ANSYS^{R15} Mechanical and assess the mechanical integrity of rotor blade in terms of stress and displacement. Figure 7 outlines the overall procedure.

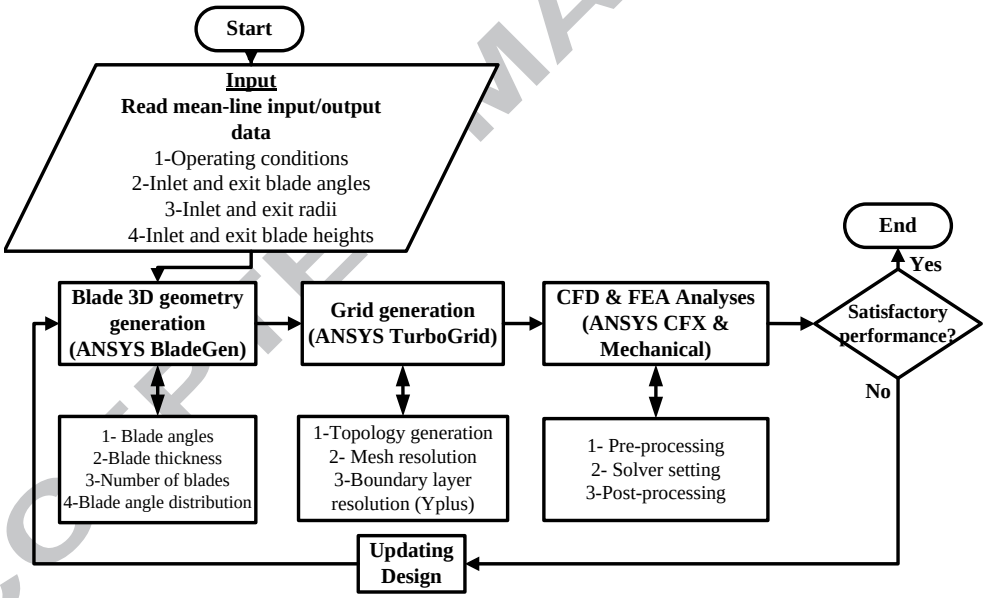

Figure 7 Schematic diagram of CFD and FEA analyses

4. 1-D Modelling and 3-D simulation results

4.1. Mean-line (1-D) parametric study results

The developed mean-line model was employed to perform parametric studies in order to investigate the effect of input variables (Table 3) on the turbine critical performance parameters (i.e. power and efficiency) and turbine size (i.e. rotor inlet diameter). Such parametric studies are based on simultaneous variation of two input parameters in a defined range (with other inputs kept constant). Such plots are then examined to determine the values of these two parameters that give the best performance. Such values will be fixed in the next

run where two other variables will be changed and this process will be repeated until the best values will be identified for all the input parameters. It is clear from Figures 8(a) and (c) that the effect of $T_{t,1}$ is more significant on the power output and d_4 than $P_{t,1}$. Following equation 1, both v and $ER_{t,s}$ are fixed, therefore increasing $T_{t,1}$ will increase U_4. Then following equation 2 and with constant ω, the larger U_4, the larger r_4 and hence the larger d_4. Figure 8(b) shows that the effect of $T_{t,1}$ is limited as increasing $T_{t,1}$ from 323K to 473K reduces stage efficiency only by 1.5%, while, increasing $P_{t,1}$ from 150kPa to 400kPa is more considerable as it reduces stage efficiency by 3.5% . Figure 9 shows that power and efficiency are increasing as the mass flow rate increases. This is directly related to the relation between mass flow rate and power as shown in Equation 4 with constant enthalpy drop. Moreover, at higher mass flow rates the temperature drop across the turbine is increasing leading to higher efficiency levels with constant expansion ratio (ER_{ts}) as illustrated by Equation 8. However, d_4 is independent of mass flow rate variation. It is only for the stage total-to-static efficiency and at lowest ER_{ts} of 1.5 that the effect of increasing flow rate is limited. As depicted in Figure igure 9(a) power is increasing as the ER_{ts} increases because of the larger actual enthalpy drop across the turbine, however, larger ER_{ts} of 3 has adverse effect of reducing stage total-to-static efficiency (Figure 9(b)) and increasing the rotor diameter (Figure 9(c)). This is due to the fact that at larger d_4 the wetted blade surface in contact with fluid increases considerably resulting in larger friction loss and hence reduces efficiency. It is evident from Figure 10 that there exists an optimum condition that yields highest power and efficiency at velocity ratio (v) of about 0.7. Moreover, these results illustrate that both power and efficiency are a strong function of v as increasing v from 0.6 to 0.9 reduces both efficiency and power by about 33% and 37.5% respectively. In contrast, efficiency and power are a weak function of ω. Figure 10 (c) shows that, effects of these parameters on d_4 is significant and as RPM increases, d_4 decreases while as v increases, d_4 increases. Figure 11 demonstrates that the effect of varying α_4 is more significant than α_5 while d_4 being completely independent of these variations. Increasing α_4 results in larger $C_{\theta,4}$ at rotor inlet as shown in Figure 4 and enhances the actual enthalpy drop and consequently power and efficiency (with fixed expansion ratio and isentropic enthalpy drop). Figure 12 presents the variation of the rotor radii ratios and it is only the stage efficiency that is noticeably affected by such variation. With fixed $r_{5,hub}/r_4$ ratio, increasing $r_{5,tip}/r_4$ results in larger A_5 based on Equation 5 and according to the conservation of mass, C_5 is reduced resulting in smaller exit kinetic losses and consequently increases the efficiency. However, at the same time increasing

$r_{5,tip}/r_{4,}$ increases the secondary losses and combination of these two effects offset the increase in efficiency curve at high $r_{5,tip}/r_4$ values.

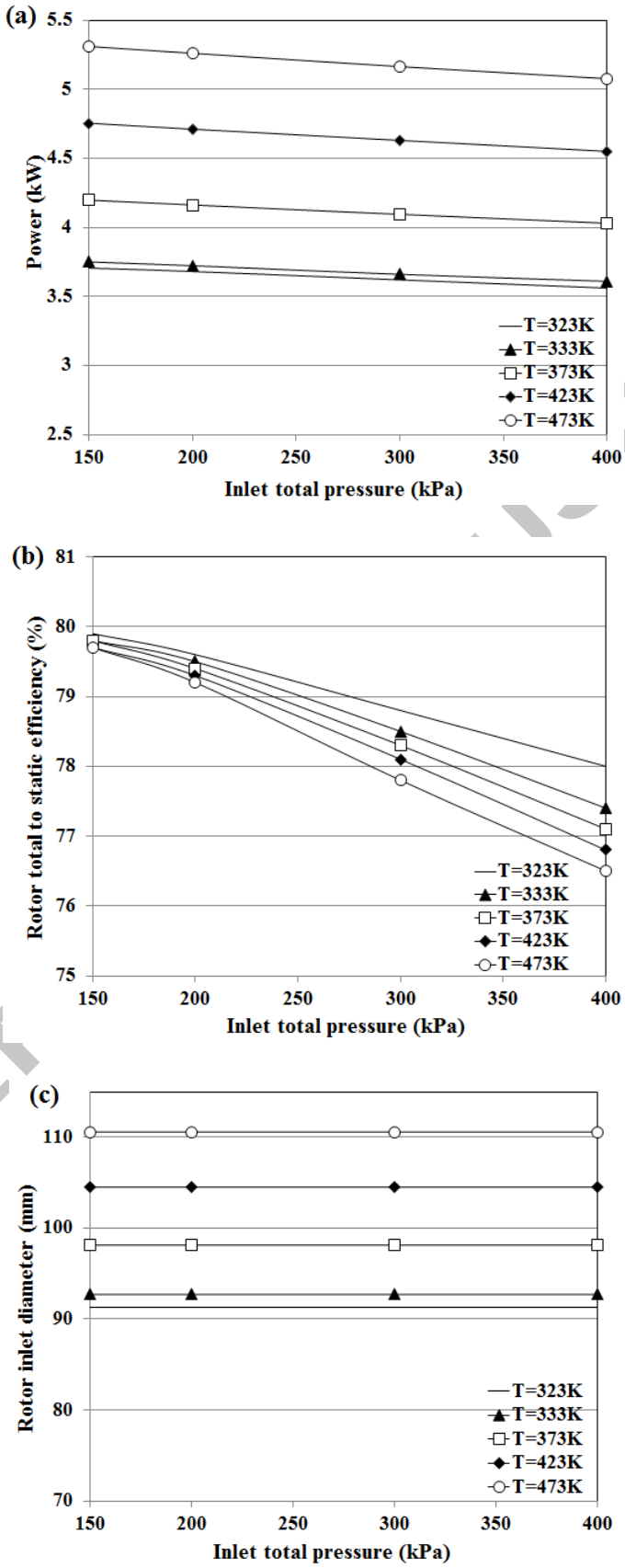

Figure 8 Effect of inlet total pressure and temperature on power, efficiency and size with ER_{ts}=2, $\dot{m}$=0.08, v_{ts} =0.7, ω=50000, α_4 =70, α_5=0, $r_{5,hub}/r_4$=0.3, $r_{5,tip}/r_4$=0.65

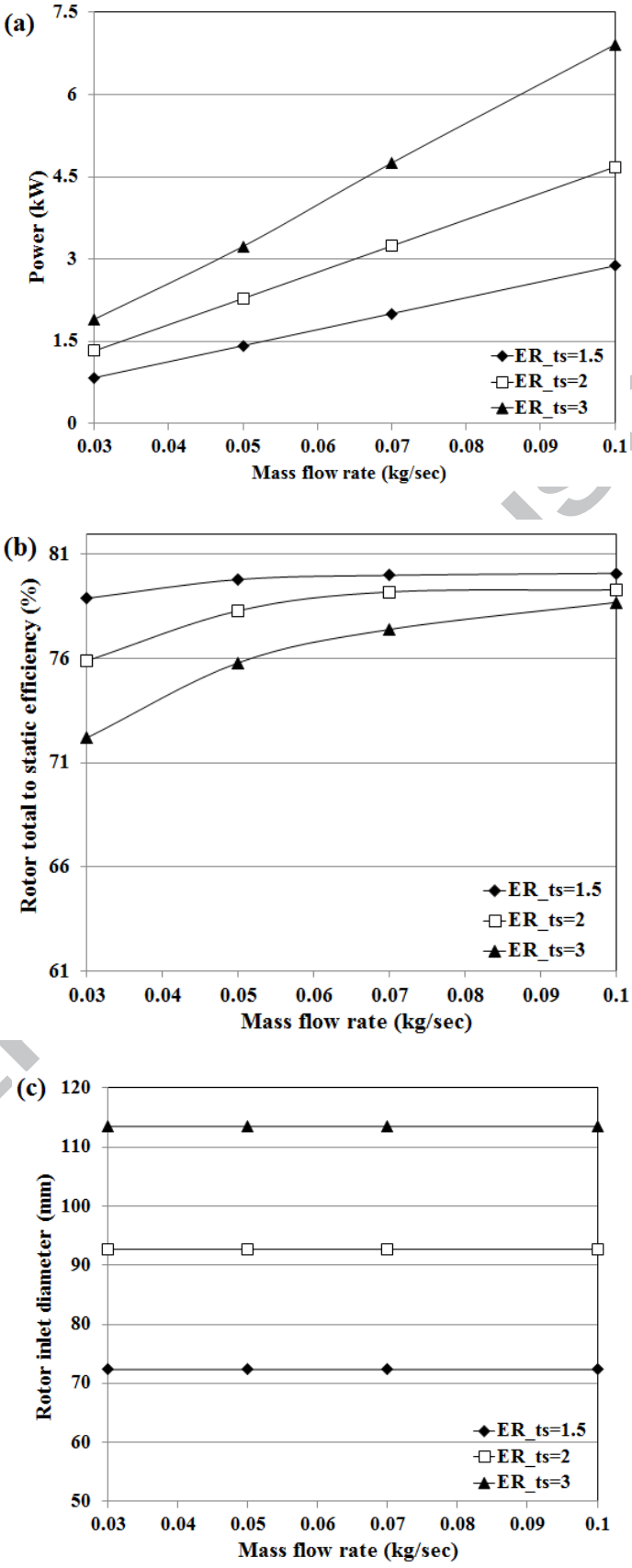

Figure 9 Effect of mass flow rate and expansion ratio on power, efficiency and size with $T_{t,1}$=323K $P_{t,1}$=200kPa , v_{ts}=0.7, ω=50000, α_4=70, α_5=0, $r_{5,hub}/r_4$=0.3, $r_{5,tip}/r_4$=0.65

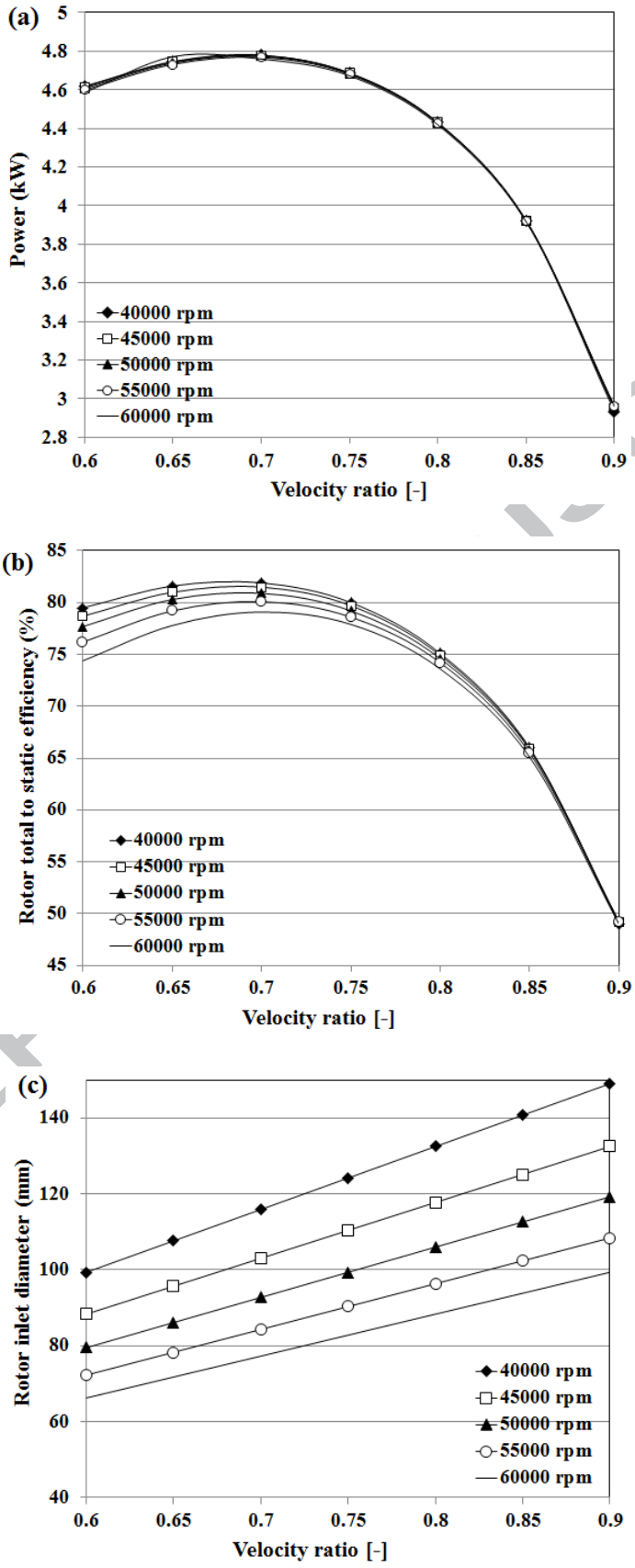

Figure 10 Effect of velocity ratio and rotational speed on power, efficiency and size with $T_{t,1}$=323K $P_{t,1}$=200kPa , ER_{ts}=2, $\dot{m}$=0.09, α_4=70, α_5=0, $r_{5,hub}/r_4$=0.3, $r_{5,tip}/r_4$=0.65

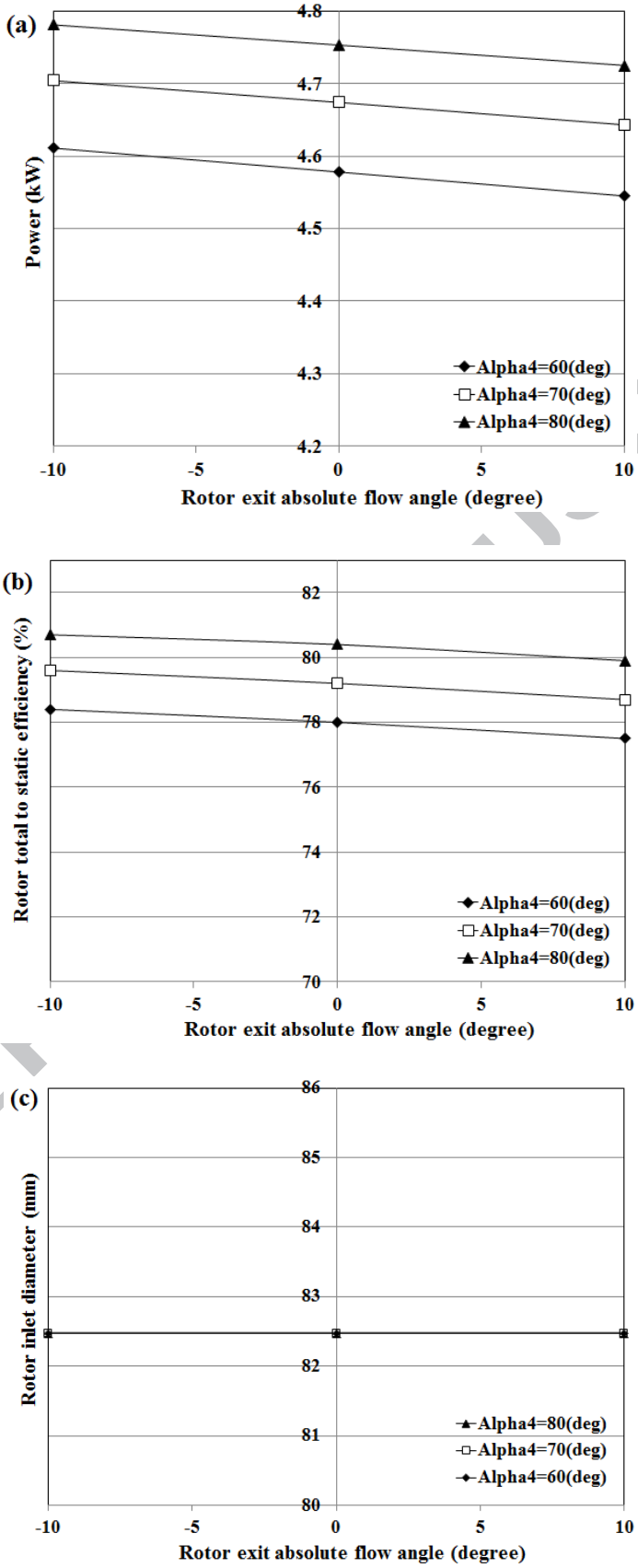

Figure 11 Effect of rotor inlet and exit absolute flow angles on power, efficiency and size with $T_{t,1}$=323K $P_{t,1}$=200kPa , ER_{ts}=2, $\dot{m}$=0.09, v_{ts}=0.68, ω=55000, $r_{5,hub}/r_4$ =0.3, $r_{5,tip}/r_4$=0.65

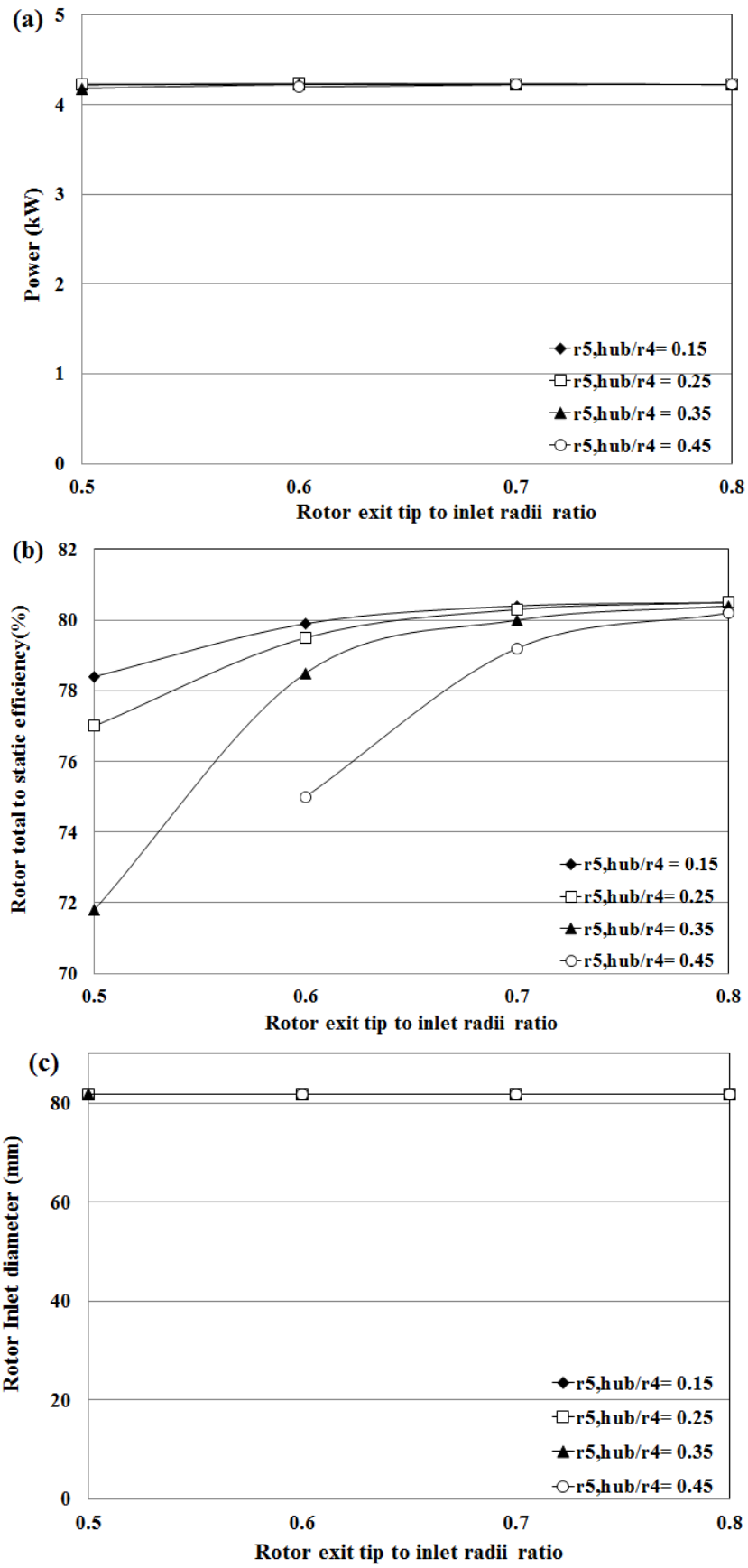

Figure 12 Effect of rotor radii ratio on power, efficiency and size with $T_{t,1}$=323K $P_{t,1}$=200kPa , ER_{ts}=2, $\dot{m}$=0.09, v_{ts}=0.68, ω=55000, α_4=78.6, α_5=0

Selected values of all investigated input parameters and corresponding mean-line modelling results are summarized in Tables 4 and 5. Performance parameters obtained by mean-line model are in the favouring operating region of the RIT and underlines the rationale selection of this configuration for CAES application.

Table 4 Selected turbine design input parameters

Parameter	Selected value
Inlet total temperature ($T_{t,1}$)	323
Inlet total pressure ($P_{t,1}$)	200
Expansion ratio (ER_{ts})	2
Mass flow rate ($\dot{m}$)	0.09
Velocity ratio (v_{ts})	0.68
Rotational speed (ω)	55000
Rotor inlet absolute flow angle (α_4)	78.6
Rotor exit absolute flow angle (α_5)	0
Rotor exit hub to inlet radii ratio ($r_{5,hub}/r_4$)	0.2
Rotor exit tip to inlet radii ratio ($r_{5,tip}/r_4$)	0.55

Table 5 Mean-line modelling results

Parameter	Unit	Value
Thermodynamic properties		
Rotor inlet total pressure ($P_{t,4}$)	kPa	194.12
Rotor inlet total temperature ($T_{t,4}$)	K	323
Rotor inlet static pressure (P_4)	kPa	152.38
Rotor inlet static temperature (T_4)	K	301.4
Rotor exit total pressure ($P_{t,5}$)	kPa	102.21
Rotor exit total temperature ($T_{t,5}$)	K	275.9
Rotor exit static pressure (P_5)	kPa	100
Rotor exit static temperature (T_5)	K	274.2
Geometry parameters		
Rotor inlet diameter (d_4)	m	0.080634
Rotor inlet blade height (b_4)	m	0.004979
Rotor exit tip diameter ($d_{5,tip}$)	m	0.04435
Rotor exit hub diameter ($d_{5,hub}$)	m	0.01613
Rotor exit area (A_5)	m^2	0.001206
Rotor axial length ($l_{rotor,x}$)	m	0.02117
Rotor blade number (Z_{rotor})	-	16
Nozzle inlet diameter (d_2)	m	0.10564
Nozzle exit diameter (d_3)	m	0.0845
Nozzle pitch (S_{nozzle})	m	0.01015
Nozzle total throat area ($A_{throat,total}$)	m^2	0.000249
Flow velocities and angles		
Rotor inlet wheel velocity (U_4)	m/s	232.21
Rotor inlet relative flow angle (β_4)	degree	-39.61
Rotor inlet absolute velocity (C_4)	m/s	199.1
Rotor inlet Mach number (Ma_4)	-	0.5985
Rotor inlet relative Mach number ($Ma_{4,rel}$)	-	0.1432

Rotor inlet relative velocity (W_4)	m/s	-49.82
Rotor exit relative flow angle at hub ($\beta_{5,hub}$)	degree	-38.35
Rotor exit relative flow angle at RMS ($\beta_{5,rms}$)	degree	-60.62
Rotor exit relative flow angle at tip ($\beta_{5,tip}$)	degree	-67.04
Rotor exit absolute velocity (C_5)	m/s	58.7
Rotor exit relative velocity at RMS ($W_{5,rms}$)	m/s	-140.6
Rotor exit relative Mach number ($Ma_{5,rel,rms}$)	-	0.417
Performance parameters		
Specific speed (N_s)	-	0.409
Flow coefficient (φ)	-	0.2528
Loading coefficient (ψ)	-	0.8791
Power	kW	4.152
Total-to-static efficiency ($\eta_{stage,ts}$)	%	81.3

4.2. Computational fluid dynamics (CFD) analyses results

4.2.1. 3-D blade generation of rotor and nozzle

3-D geometry of nozzle and rotor blades are created with ANSYS[R15] BladeGen using mean-line data (Table 5) as well as blade angle and thickness distribution, stagger and metal wedge angles and nozzle throat area as shown in Figure 13.

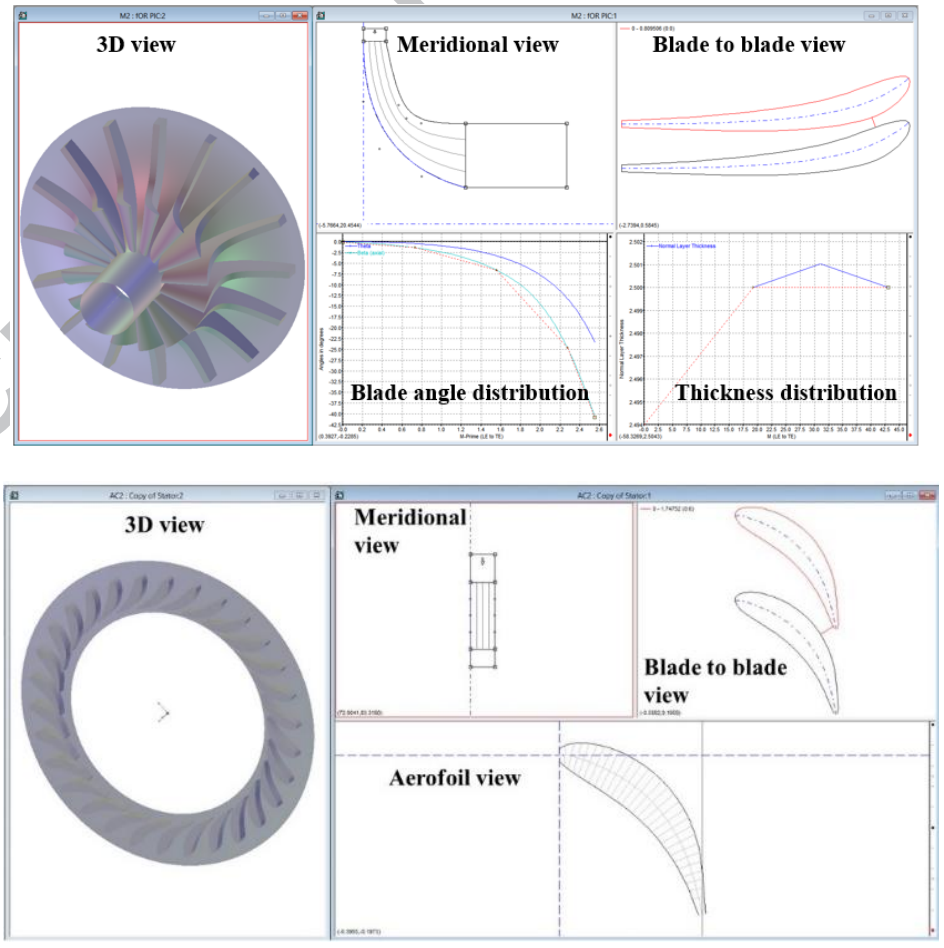

Figure 13 (Top) Rotor geometry (bottom) nozzle geometry

4.2.2. CFD setup and turbulence modelling

ANSYS CFX[R15] was employed to solve 3-D compressible viscous RANS equations using the high resolution advection scheme based on finite volume approach. Conservation of mass, momentum and energy were solved with following equations while using air as the working fluid.

$$\frac{\partial \rho}{\partial t} + \nabla.(\rho \boldsymbol{U}) = 0 \qquad \text{Equation 44}$$

$$\frac{\partial (\rho \boldsymbol{U})}{\partial t} + \nabla.(\rho \boldsymbol{U} \otimes \boldsymbol{U}) = -\nabla P + \nabla.\zeta + \boldsymbol{S}_M \qquad \text{Equation 45}$$

$$\frac{\partial (\rho h_t)}{\partial t} - \frac{\partial P}{\partial t} + \nabla.(\rho \boldsymbol{U} h_t) = \nabla.(\lambda \nabla T) + \nabla.(\boldsymbol{U}.\zeta) + \boldsymbol{U}.\boldsymbol{S}_M + \boldsymbol{S}_E \qquad \text{Equation 46}$$

Where ζ is stress tensor and is related to strain rate by:

$$\zeta = \mu\left(\nabla \boldsymbol{U} + (\nabla \boldsymbol{U})^T - \frac{2}{3}\delta\, \nabla.\boldsymbol{U}\right) \qquad \text{Equation 47}$$

For rotating frame of reference, rotating at a constant velocity of ω, additional sources of momentum are required to account for the effects of the Coriolis and centrifugal forces.

$$\boldsymbol{S}_{M,rot} = \boldsymbol{S}_{Cor} + \boldsymbol{S}_{cfg} \qquad \text{Equation 48}$$

$$\boldsymbol{S}_{Cor} = -2\rho\omega \times \boldsymbol{U} \qquad \text{Equation 49}$$

$$\boldsymbol{S}_{cfg} = -\rho\omega \times (\omega \times \boldsymbol{r}) \qquad \text{Equation 50}$$

Where $\boldsymbol{r}$ is the location vector and $\boldsymbol{U}$ is the relative frame velocity vector. In the energy equation (Equation 46) the advection and transient terms use rothalpy (I) instead of the total enthalpy (h_t).

$$I = h_{stat} + \frac{1}{2}U^2 - \frac{1}{2}\omega^2 r^2 \qquad \text{Equation 51}$$

Transport equations described above then augmented with constitutive equations for calculating density, enthalpy, specific heat capacity and entropy while assuming air as an ideal gas.

$$\rho = \frac{w\boldsymbol{P}_{abs}}{R_0 T} \qquad \text{Equation 52}$$

$$dh = C_p dT \qquad \text{Equation 53}$$

$$C_p = C_p(T) \quad \text{Equation 54}$$

Entropy depends on the equation of state and the constitutive relationship for the material. For ideal gases (which is the case of the present study) with constant C_p or C_p as a function of temperature, entropy change is calculated as below.

$$S - S_{ref} = \int_{T_{ref}}^{T} \frac{C_p(T)}{T}\, dT - R\, log\left(\frac{P}{P_{ref}}\right) \quad \text{Equation 55}$$

Where P_{ref} is the absolute pressure datum from which all other pressure values are taken and the default reference state for T_{ref} is 0 K. For general functions for C_p the solver computes an entropy table as a function of both temperature and pressure. In the simplified case when C_p is a constant, the following analytical formula is used.

$$S - S_{ref} = C_p log\left(\frac{T}{T_{ref}}\right) - R\, log\left(\frac{P}{P_{ref}}\right) \quad \text{Equation 56}$$

For the cases that the working fluids have strong real gas behaviour such as the ORC, real gas equation of states (i.e. Aungier Redlich Kwong or Peng Robinson) will be employed by CFX as shown in the study conducted by [32]. For turbulence modelling the shear stress transport (SST) turbulent flow model was employed. The advantage of using SST compared with others is the capability of automatic near-wall treatment for locating the first node away from wall (Y^+) to capture turbulence closure. Additionally, since the flow in RIT is turbulent with flow separation and strong pressure gradients, SST model can accurately predict the onset and the amount of flow separation under adverse pressure gradients in contrast to *k-ε* model that under-predict such phenomena. SST developed by [33] is suitable for high accuracy boundary layer simulations which combines the original Wilcox *k-ω* and *k–ε* models. SST uses *k-ω* formulation in the inner parts of the boundary layer that makes the model directly usable all the way down to the wall through the viscous sub-layer and then switches to a *k-ε* behaviour in the free-stream. Such model is very practical for aerodynamic investigation of turbomachines and has a wide range of applications in the industry. Details of such model can be found in [33]. Inlet total temperature and pressure were set as the boundary conditions at the nozzle inlet (assuming negligible losses in the casing) while static pressure was set at the rotor outlet and it was assumed that the upstream flow approaches the nozzle in the perpendicular direction (radial direction). A mixing plane model (stage interface) was applied at the nozzle-rotor interface to provide communication across the stationary and rotating blade row domains. CFD analyses were conducted for one rotor blade passage and two nozzle blade passages to obtain the pitch angle ratio of around unity and

results are assumed to represent the complete nozzle and rotor wheels due to periodicity. The nozzle domain has no tip clearance while the rotor domain includes a tip clearance of 0.56mm obtained from the mean-line modelling. In addition, all the walls are assumed to be smooth, adiabatic with no-slip conditions. CFX solver convergence criterion was set to 10^{-5} for all the residuals with the physical timescale of $0.5/\omega$ as suggested in the CFX user manual and all analyses were carried out at the steady state condition. Figure 14 outlines details of computational fluid domains. Inlet and exit fluid domains are extended about one and half axial chord length of nozzle and rotor respectively to improve numerical stabilization as suggested in [34].

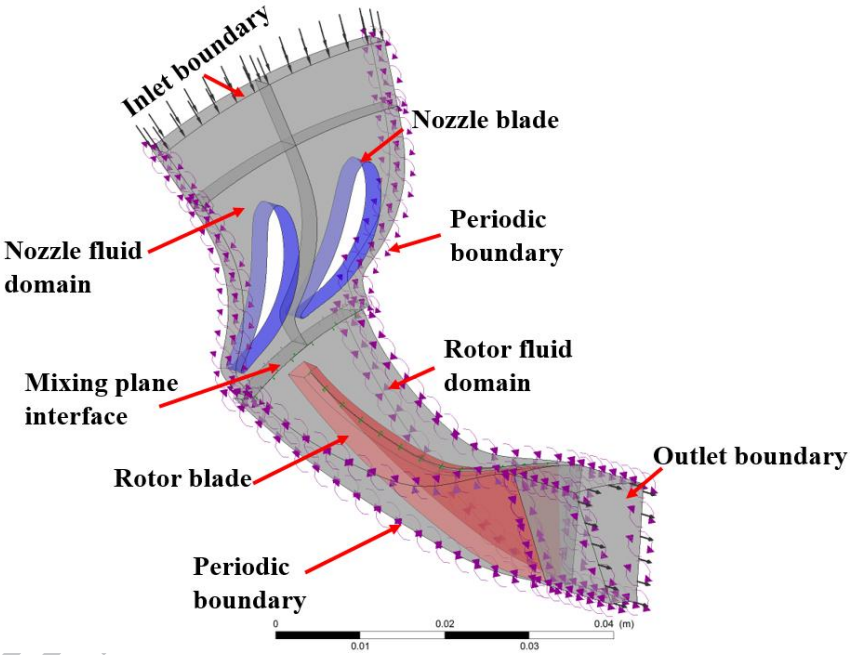

Figure 14 Computational fluid domains for nozzle and rotor

4.2.3. Grid sensitivity analysis

Grid independence study was carried out by adding more elements in the hub-to-tip and blade-to-blade directions because the Y^+ variation depends on the first grid spacing to a wetted surface in those two directions. Table 6 presents the results of such study.

Table 6 Grid sensitivity study results

	Number of elements		Stage total-to-static efficiency (%)	Power output (kW)	Mass flow rate (kg/s)	Y^+ (b)	Global imbalance (c) (%)	CPU time (min)
	Nozzle(a)	Rotor						
1	20280	30384	80.727	4.6	0.0974	31.34	0.00015	4
2	97768	318356	81.48	4.366	0.0919	6.08	0.00265	12
3	247680	448972	81.95	4.356	0.0912	3.24	0.0716	22

4	400608	911378	82.15	4.366	0.0911	1.67	0.0314	38
5	597042	1848809	82.25	4.370	0.0911	0.9015	0.0092	74

(a) The number of nozzle elements is per passage.
(b) The Y^+ values are averaged throughout the nozzle and rotor blade passages.
(c) The global imbalance values are averaged throughout the nozzle and rotor blade passages. Global imbalance is the domain imbalances that are generated for all transport equations including mass, momentum and energy except for turbulence equations that have special wall treatment according to the ANSYS CFX solver manager guide

As it is clear from Table 6, all the global imbalances are much less than 1% which confirms proper solver convergence as suggested in the CFX solver theory guide. Y^+ (boundary layer mesh size) is required to be around unity for the K-ω based SST turbulent flow model as suggested in CFX user's manual. The larger the number of elements both in the rotor and nozzle passage the lower the Y^+ value and closer to the desired range.

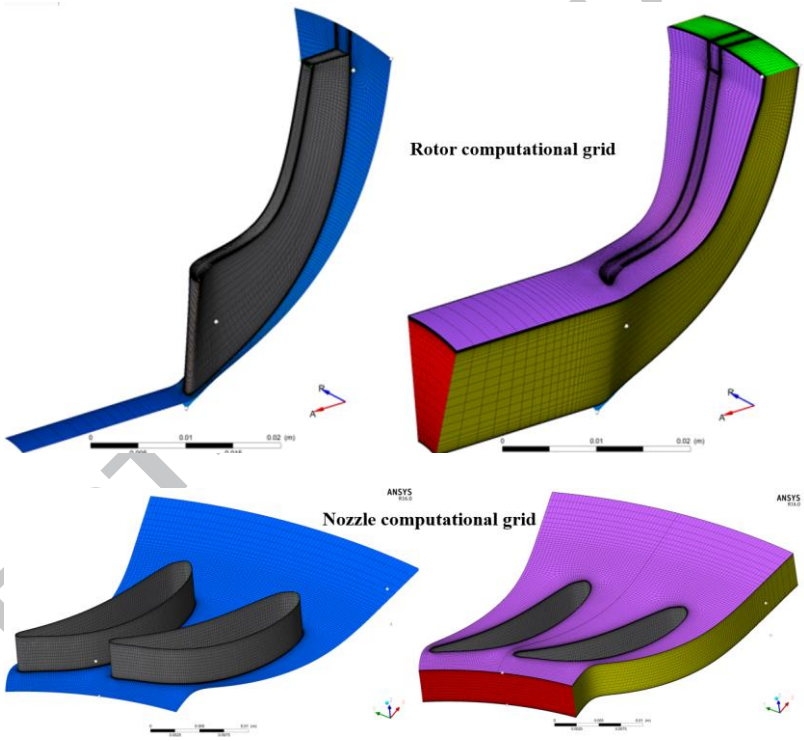

Figure 15 Selected grid size for the nozzle and rotor blade passages

Among the investigated grid resolutions, the values in rows 4 and 5 provided the least variation in efficiency, power and mass flow rate together with the Y^+ value that is in the suggested range. However, there exists noticeable difference in CPU time that increases significantly as Y^+ value decreases. Therefore, as a compromise between the accuracy of results, grid independence and computational time, grid size in the fourth row of Table 6 was selected and shown in Figure 15.

4.2.4. Effect of blade angle distribution

The principal focus of aerodynamic evaluations was the bladed regions of RIT, with the rotor having the highest priority. Various rotor blade shapes will be analysed and based on their quantitative (efficiency and power) and qualitative (velocity vectors, entropy contours and blade loading) results, the most favourable configuration will be selected (nozzle geometry kept fixed).

Four different blade profiles (Figure 16) were investigated with the aim of achieving uniform flow with minimal secondary losses and least entropy generation rate (highest isentropic efficiency). Blade profile "A" has a very small turning angle in the large portion of the passage and very sharp turning around the exit, blade profile "B" has significant turning in the first part of passage and small turning at the exit, blade profile "C" has modest blade turning angle along the whole length of passage while blade profile "D" is the combination of profiles "A" and "C".

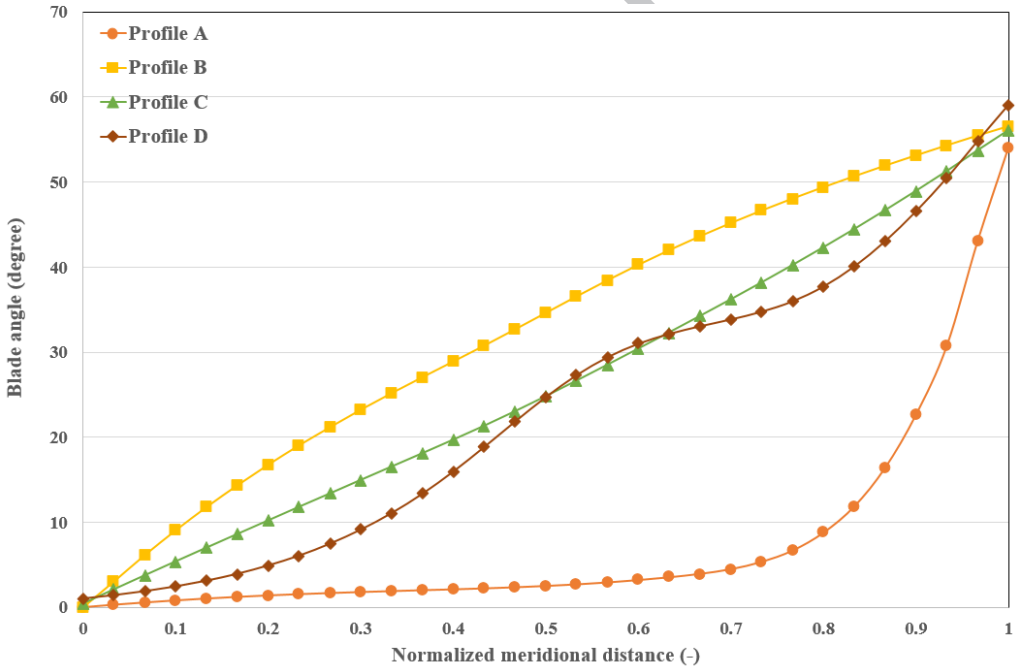

Figure 16 Blade angle distribution at half span for 4 different blade profiles

Figures 17 to 20 show the blade-to-blade velocity vectors at half span for the four different blade profiles. All configurations have 16 rotor blades as suggested by Equation 16. As shown in Figure 18 there exist noticeable flow separation together with strong secondary flows on the pressure surface (PS) of profile "B" just downstream of the leading edge. Such flow characteristics also exist in the profile "C" as shown in Figure 19 but the intensity of the local flow circulation has been reduced considerably and flow expands smoothly after this

region. Development of such secondary flows on the PS at the rotor inlet region of profile "D" was substantially reduced with a preferential flow pattern for the remainder of passage as presented in Figure 20. Although profile "A" seems appealing as there is no evidence of secondary flow (Figure 17), such profile was unable to accelerate W_5 to high levels in majority of rotor passage with the maximum value of 86.03 m/s compared to 121.7m/s, 116.32m/s and 111.6m/s for profiles "B", "C" and "D" respectively. On the other hand, the largest W_5 for profile "B" resulted in largest C_5 of 88.13m/s and hence the largest exit kinetic loss compared to 83.06m/s and 80.87m/s for profiles "C" and "D" respectively. More importantly, due to the low flow velocity levels the viscous shear force became dominant in the passage of profile "A" and results in high level of entropy generation in large portion of passage as shown by the entropy contour plot in Figure 21. Comparing the entropy distribution contours for all four profiles (Figures 21 to 24) revealed that the level of entropy generation in profile "D" was the lowest. Such characteristic is the principal reason for the profile "D" to exhibit the highest efficiency of 83.33% compared to other profiles as summarized in Table 7. Although profile "C" has competitive performance (82.57%), the subtle variation in the blade angle distribution of the blade profile "D" resulted in noticeable reduction in entropy generation as it is evident in Figures 23 and 24. Moreover, the CFD predicted mass flow rate and power (Table 7) for the blade profile "D" are in very good agreement with the mean-line design values of 0.09kg/s and 4.152kW respectively. Thus, the profile "D" was selected as the best configuration for further investigation.

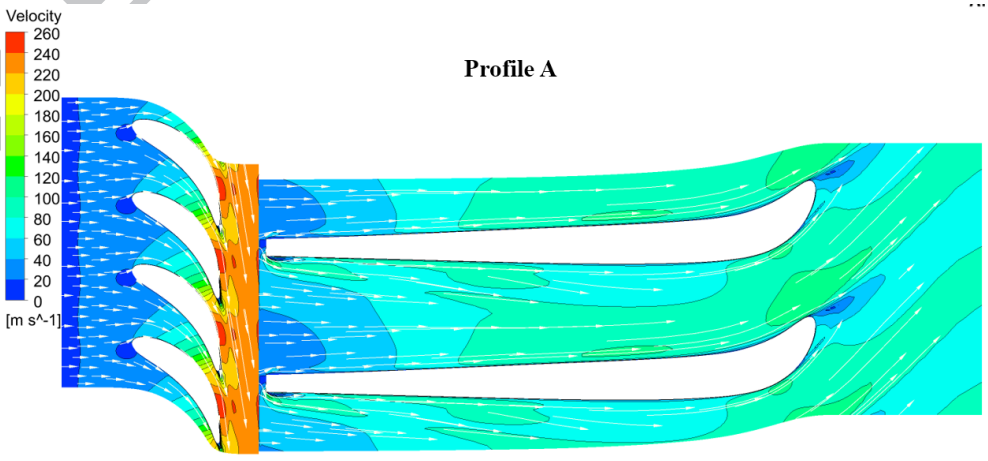

Figure 17 Velocity vectors at half span for the blade profile "A"

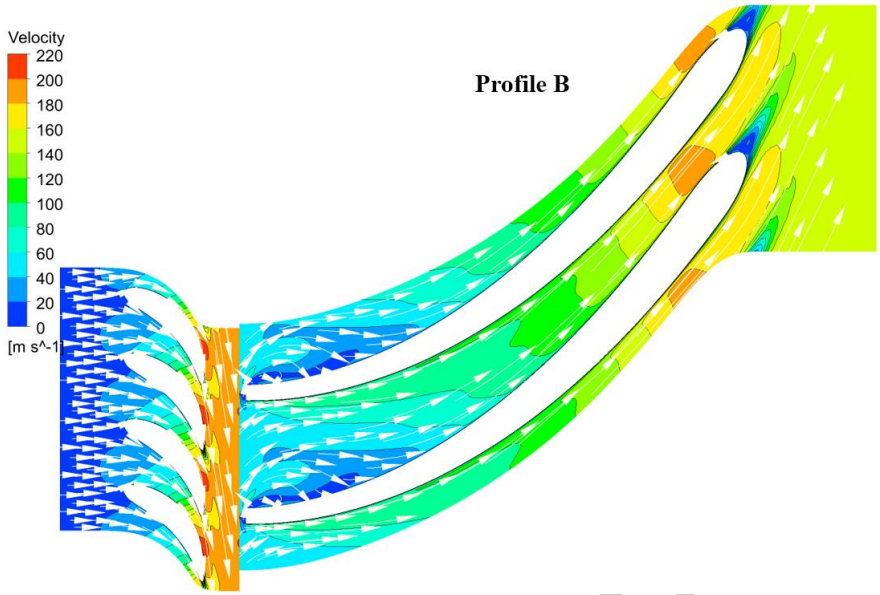

Figure 18 Velocity vectors at half span for the blade profile "B"

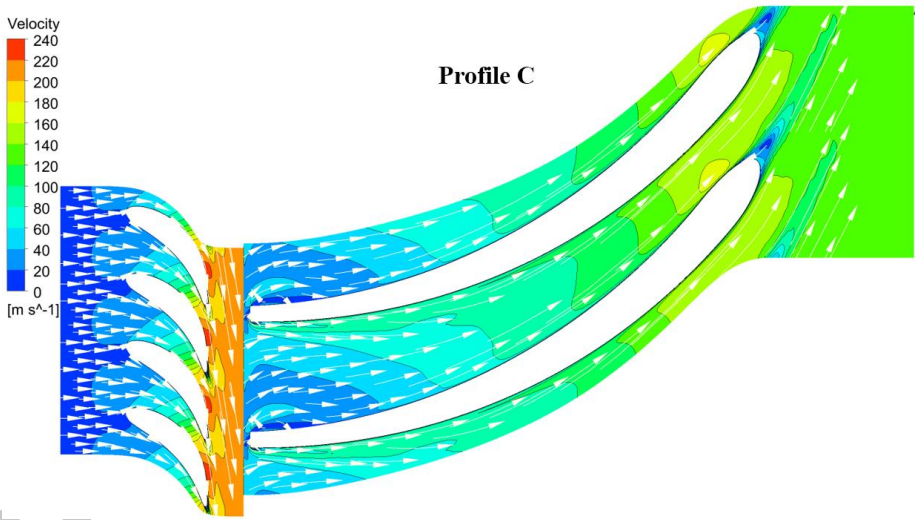

Figure 19 Velocity vectors at half span for the blade profile "C"

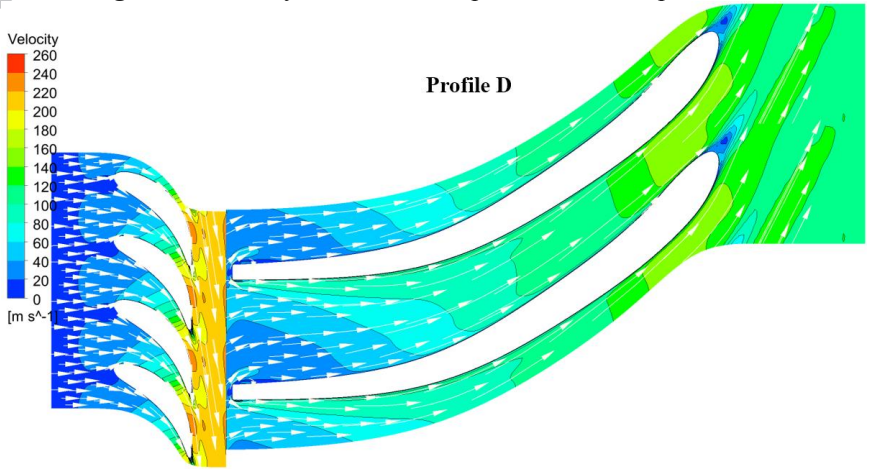

Figure 20 Velocity vectors at half span for the blade profile "D"

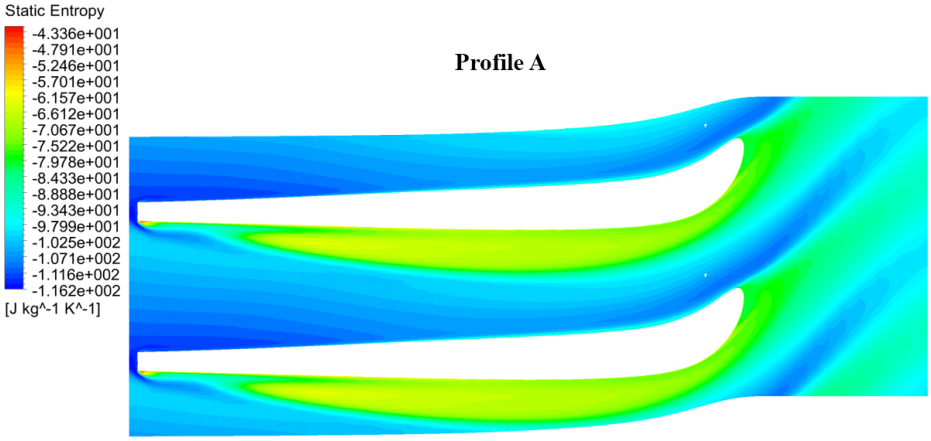

Figure 21 Contours of entropy distribution at half span for the blade profile "A"

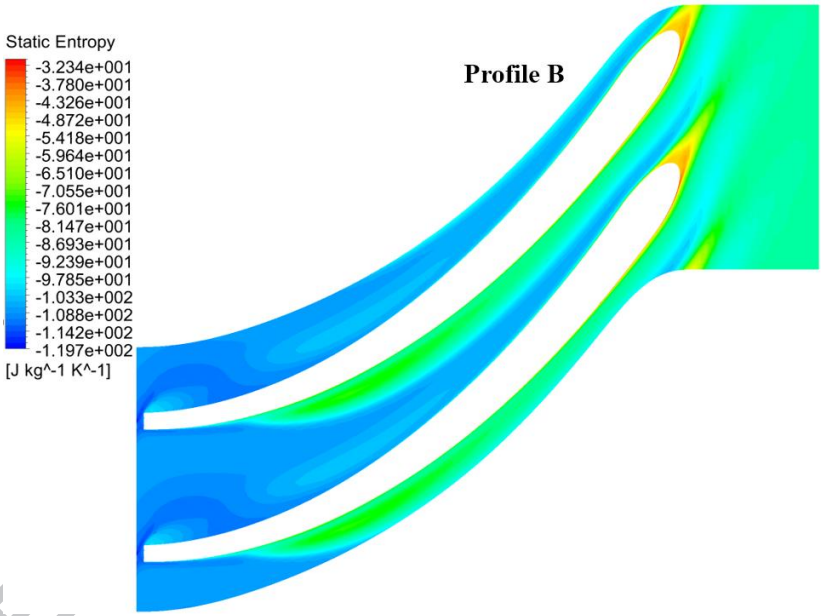

Figure 22 Contours of entropy distribution at half span for the blade profile "B"

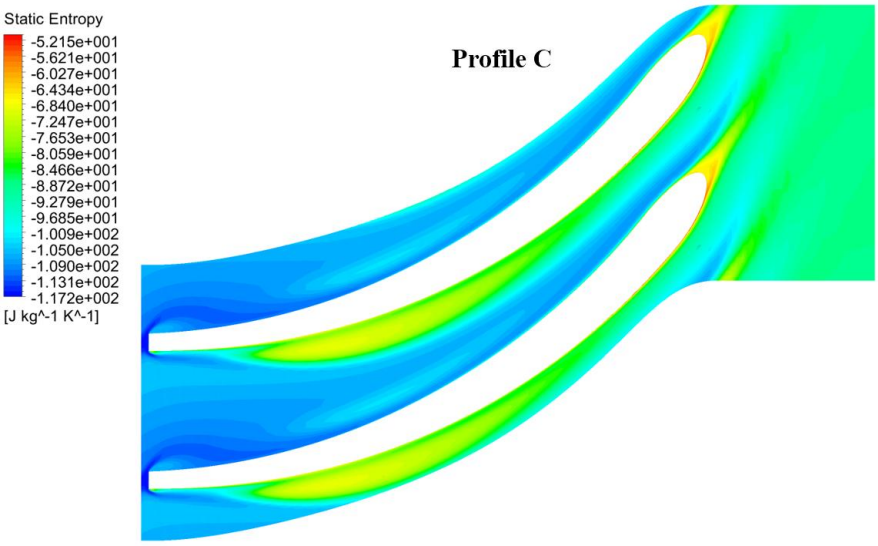

Figure 23 Contours of entropy distribution at half span for the blade profile "C"

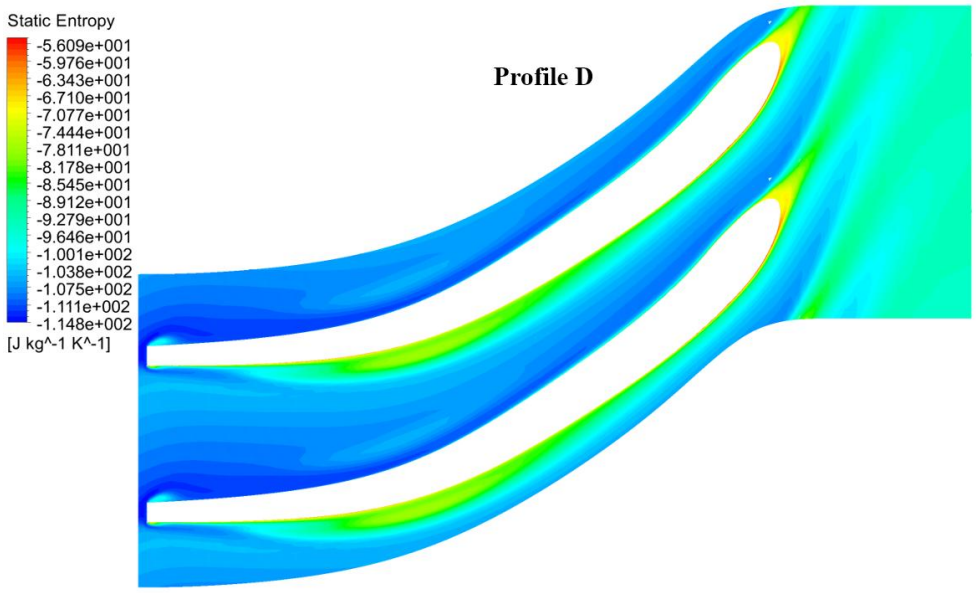

Figure 24 Contours of entropy distribution at half span for the blade profile "D"

Table 7 Summary of main performance parameters from CFD analyses of 4 investigated blade profiles

	Stage total-to-static efficiency (%)	Power (kW)	Mass flow rate (kg/s)
Profile A	82.15	4.366	0.0911
Profile B	78.58	3.675	0.0801
Profile C	82.57	4.092	0.085
Profile D	83.33	4.190	0.0863

4.2.5. Effect of blade thickness and leading edge (LE) profiles

For the blade profile "D" the effect of varying thickness distribution from hub-to-tip and also effect of the rotor LE shape were investigated. For all the CFD analyses in section 4.2.4, thickness was kept constant with the value of about 2mm from hub-to-tip as illustrated in Figure 25(a). From the aerodynamic point of view, the lower the thickness the better the performance subject to structural analysis. Therefore, for the modified case rotor blade hub-to-tip thickness is reduced linearly from about 2mm near the hub to about 1mm near the blade tip as depicted in Figure 25(b). At the same time, the shape of the rotor blade LE is changed from a square cut-off shape to a curved elliptical shape as shown in Figure 26. CFD analysis results in stage efficiency, power and mass flow rate of 84.51%, 4.343kW and 0.0884kg/s respectively. Apparently the implemented modifications improved turbine efficiency by about 1.18% while the power was increased by about 153W. Such improvement is firstly due to the shape of rotor LE for the original case with flow blockage at rotor inlet and consequently a recirculation zone (shown by red arrow in Figure 27(a)) that occupied a small

portion of the inlet passage as depicted by the velocity streamlines. However, the modified LE shape reduced the flow blockage and almost entirely eliminated the formation of flow reversal as illustrated by Figure 27(b). Furthermore, reduction in the blade thickness increased the effective flow area compared to the original case (considering the growth of the boundary layer blockage on the blade surfaces and end walls for both cases) and therefore slightly larger mass flow rate was predicted by the CFD for the modified case (0.0884kg/s) compared to the original case (0.0863kg/s). However, even with larger mass flow rate the average value of absolute flow velocity (C_5) at rotor outlet for the modified case (56.86m/s) was slightly lower than the original case (57.4m/s) as shown in Figure 28. This is due to the fact that with growth of boundary layer in the original case where the effective flow area was smaller, the flow was required to move with higher velocity in order to conserve mass and hence led to larger exit kinetic loss. The accumulative effects of these two factors resulted in better performance for the modified thickness and selected for further analyses.

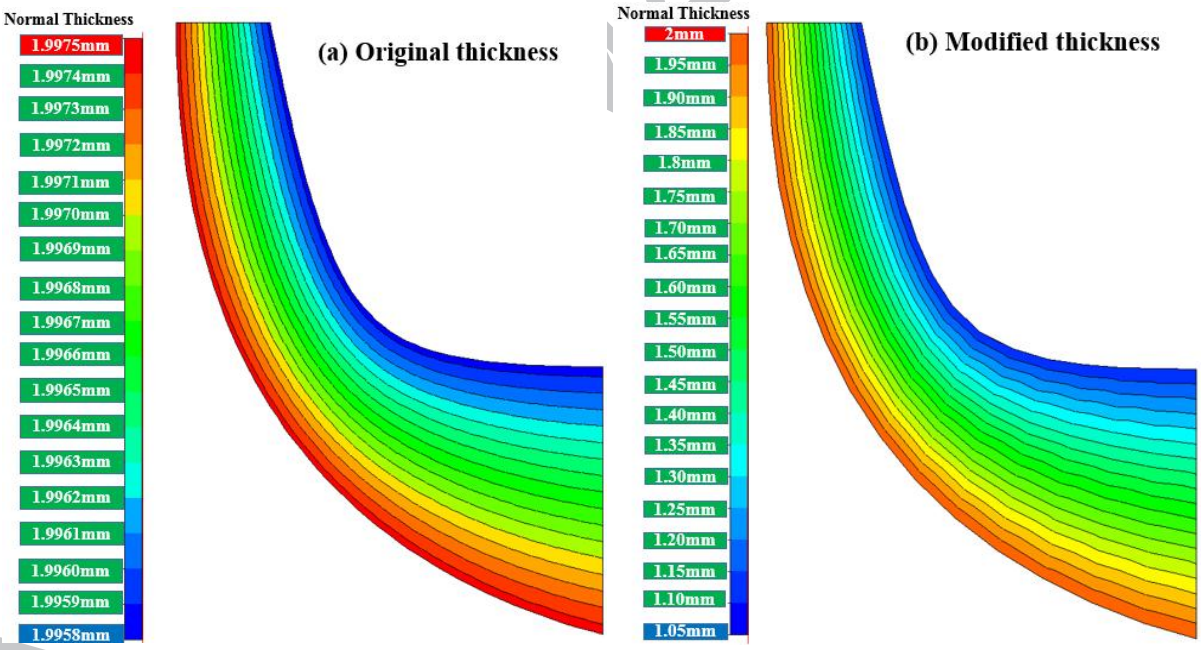

Figure 25 Variation of hub-to-tip blade thickness (a) Original thickness, (b) Modified thickness

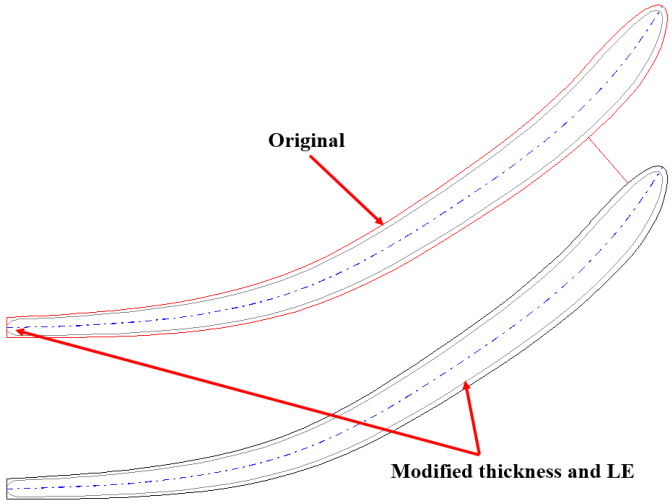

Figure 26 Blade-to-blade view of the original and modified thicknesses and LE shapes at half span

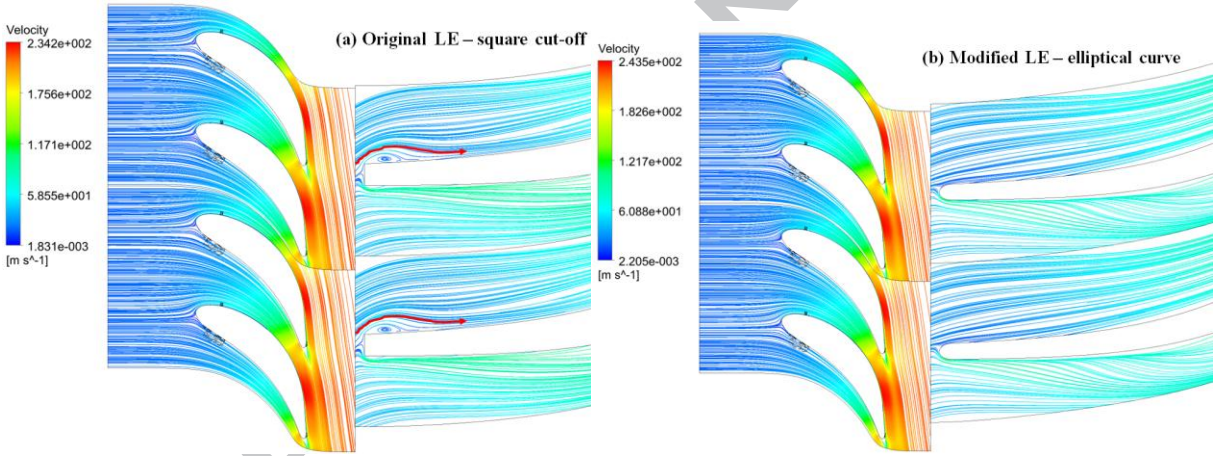

Figure 27 Velocity streamlines at half span (a) original LE – square cut-off (b) modified LE – elliptical curve

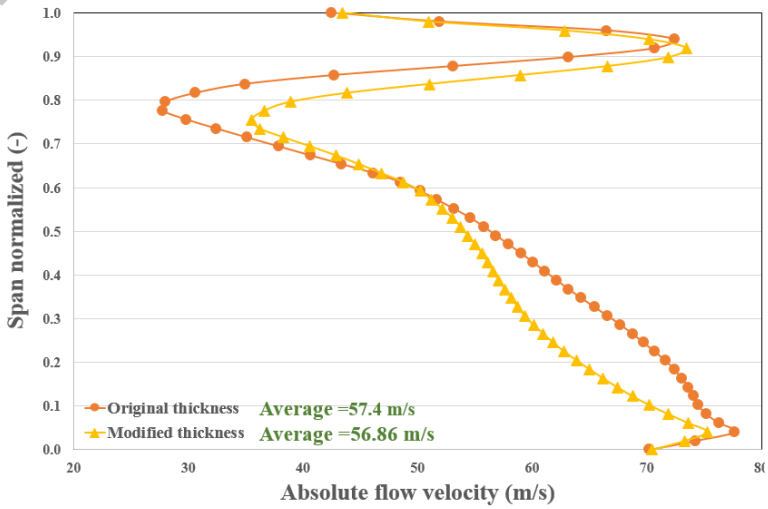

Figure 28 Absolute flow velocity (C_5) at the rotor outlet for the original and modified profile "D"

4.2.6. Effect of rotor blade number

The minimum number of rotor blades is a critical parameter that affects the performance, blade loading and rotating inertia of RIT. Despite a number of empirical correlations (i.e. Equation 16), accurate estimation of the minimum number of rotor blades that leads to best performance can be reliably obtained with CFD analyses. Profile "D" with modified thickness and LE shape was investigated for Z_{rotor} =11, Z_{rotor} =13 and Z_{rotor} =15 compared to the original value of Z_{rotor}=16. Comparing the results in Figures 29 to 32, maximum efficiency of 84.54% was obtained with Z_{rotor}=15 as shown in Figure 31.

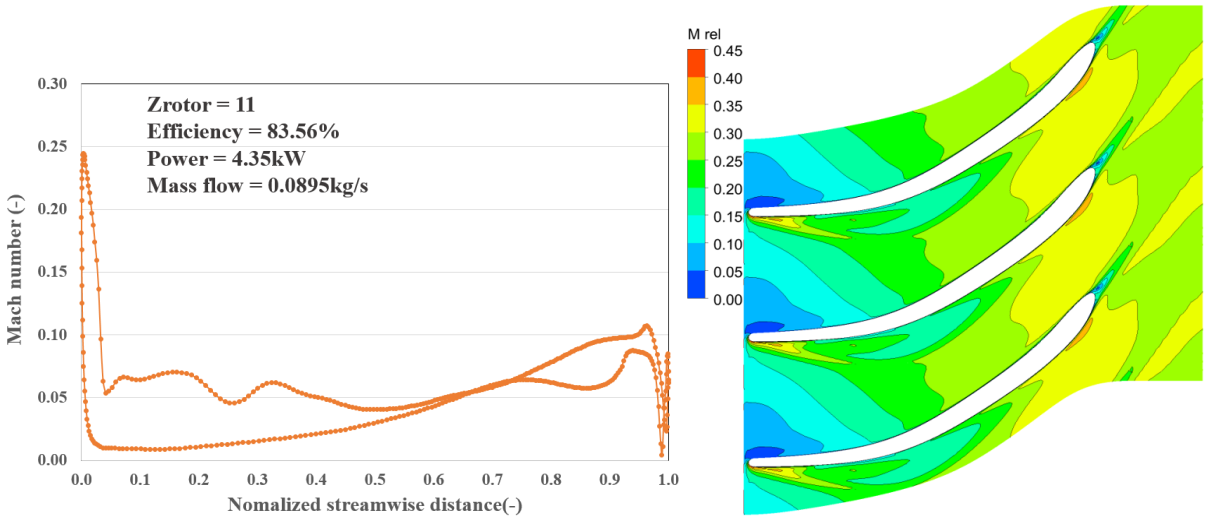

Figure 29 Blade loading (left) and Mach number (right) for Z_{rotor} =11

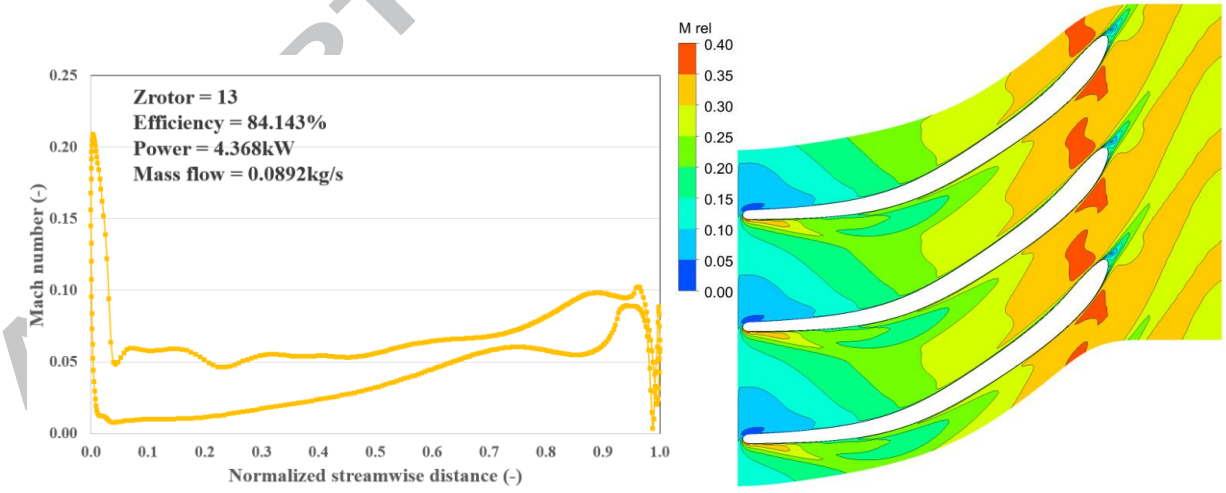

Figure 30 Blade loading (left) and Mach number (right) for Z_{rotor} =13

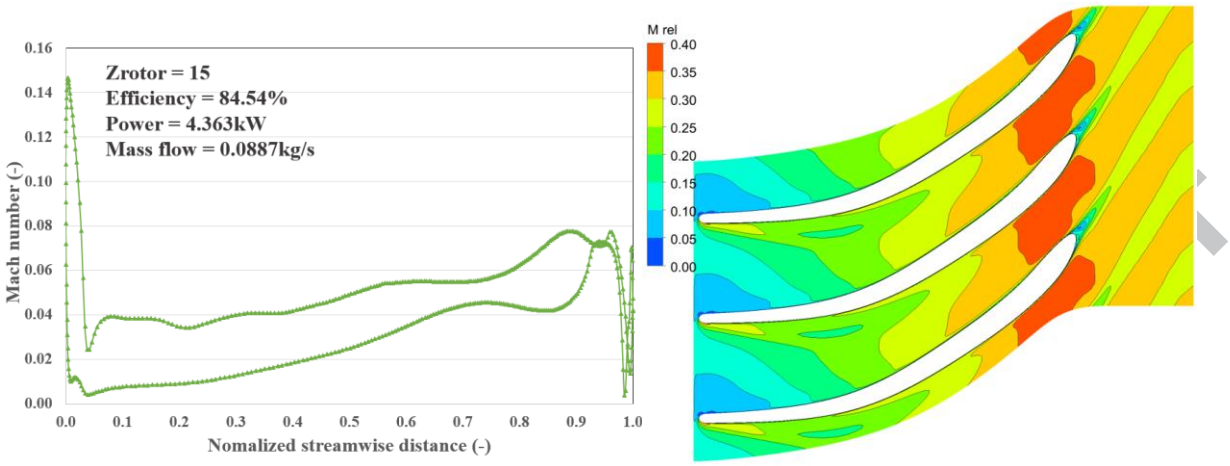

Figure 31 Blade loading (left) and Mach number (right) for Z_{rotor} =15

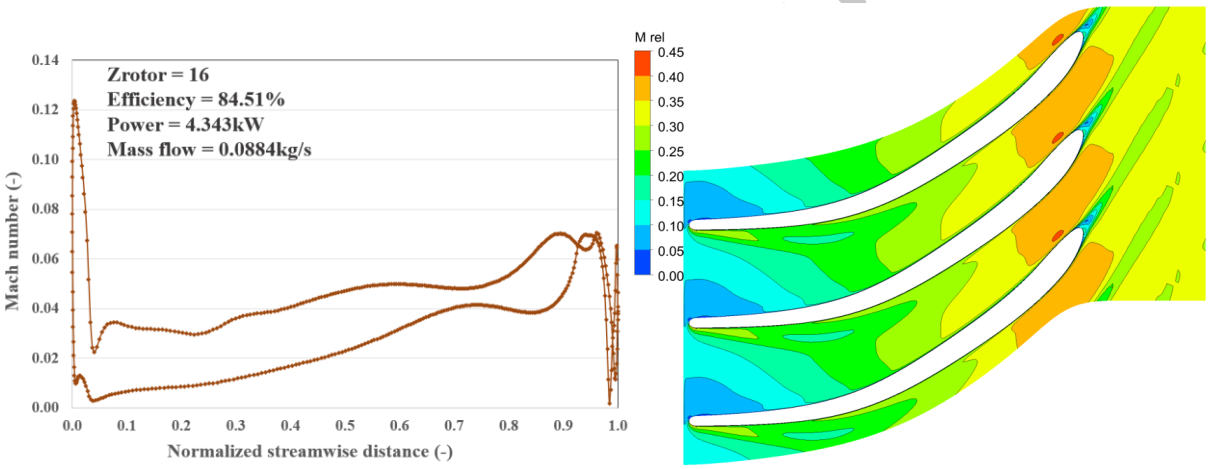

Figure 32 Blade loading (left) and Mach number (right) for Z_{rotor} =16

The case with Z_{rotor}=11 suffers from strong secondary flow and flow separation on the suction surface (SS) starting from downstream of LE and propagating to about 65% of the stream-wise passage length. Such effect is clearly visible from the blade loading chart (Figure 29) with excessive diffusion and almost negative loading. For other cases there is no evidence of negative loading. Since the aim of rotor blade is to increase the relative Mach number, both cases with Z_{rotor} =11 and 13 are unable to accelerate the flow relative velocity and therefore the relative Mach number to as high as 0.417 (Table 5) compared to Z_{rotor} =15 and 16. As can be seen, a major part of the rotor passage near the trailing edge (TE) is occupied with Mach number contour of about 0.4 for Z_{rotor} =15 and 16. Since maximum efficiency is obtained by Z_{rotor}=15 and it provided smooth expansion on both SS and PS with uniform velocity vectors and even slightly larger power output compared to Z_{rotor} =16, such value was

selected. Moreover, Z_{rotor} =15 assures that the number of rotor and nozzle blades are odd and even respectively in order to avoid the possible resonances due to the blades interaction.

It is clear that, CFD analyses can be used to predict a more realistic rotor design in terms of blade profile shape, thickness distribution and number of blades. Therefore, the blade profile "D" with the modified thickness and elliptical LE shape and Z_{rotor} =15 was selected for FEA, manufacturing and experimental testing.

Complementary results in terms of pressure, Mach number and entropy distribution along meridional channel of the case with Z_{rotor} =15 are shown in Figure 33. Clearly, there is smooth expansion in the nozzle and rotor across meridional channel of the final geometry. The entropy propagation is in accordance with the blade-to-blade plots (Figure 24). There exists slight rise in entropy especially at inlet portion of rotor passage due to formation of weak flow reversal on the PS just downstream of rotor's LE. However, entropy increases significantly at the outlet region of rotor near tip where tip leakage flow travelling away from the SS mixed out with rotor TE wake and increases loss.

Figure 34 presents the 3-D velocity streamlines within the nozzle and rotor passages and illustrates uniform flow velocity. Figure 35 shows the final 3-D geometry of the rotor and nozzle imported into a CAD package.

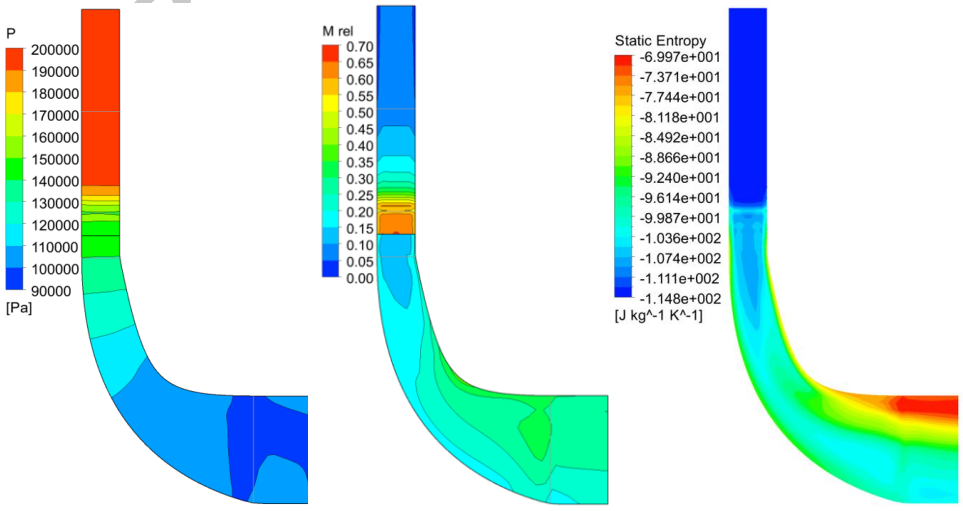

Figure 33 Meridional pressure (left), Mach number (middle) and entropy (right) distribution contour plots

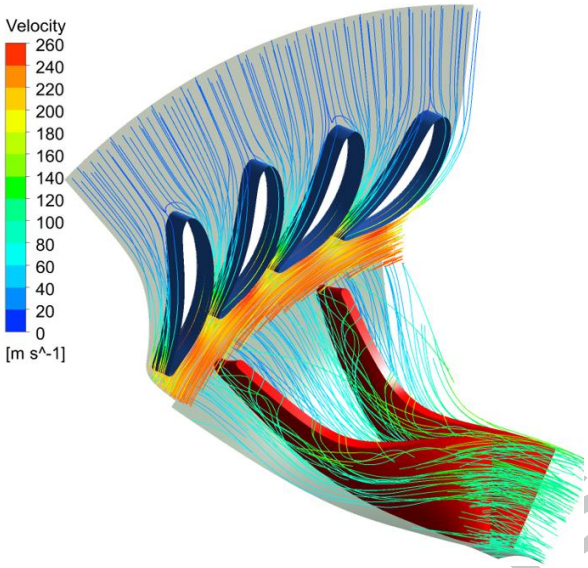

Figure 34 3-D velocity streamlines within nozzle and rotor passages

Figure 35 Final 3-D geometry of the rotor and nozzle

4.2.7. CFD analysis of the complete turbine stage

Due to the shape of the nozzle, an annular plenum with constant cross section was developed to transfer the fluid around the periphery of the nozzle (Figure 36). The casing is supposed to provide the flow to the nozzle with minimal pressure loss, appropriate incidence angle and low gas velocity. The mesh independence study for obtaining the minimal pressure variation from inlet to outlet resulted in total of 187145 tetrahedron elements as shown in Figure 37.

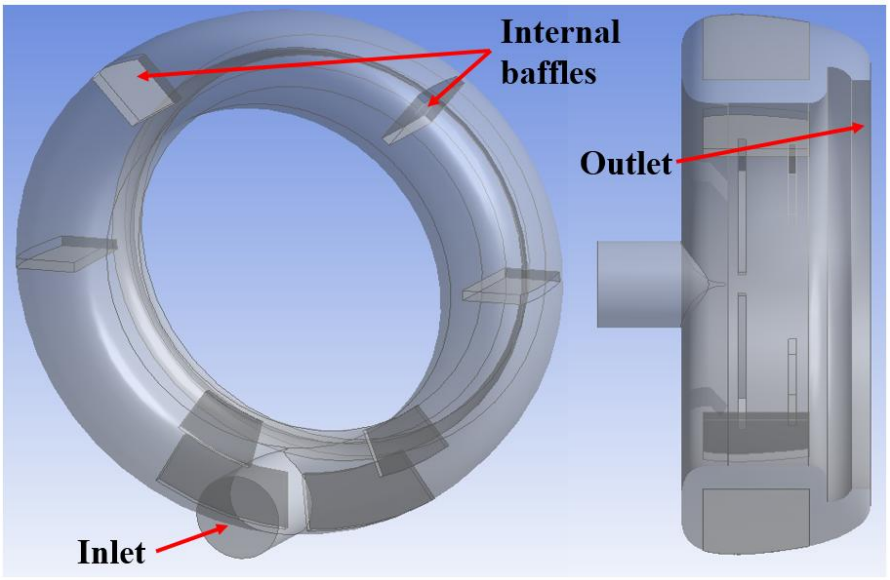

Figure 36 Casing geometry

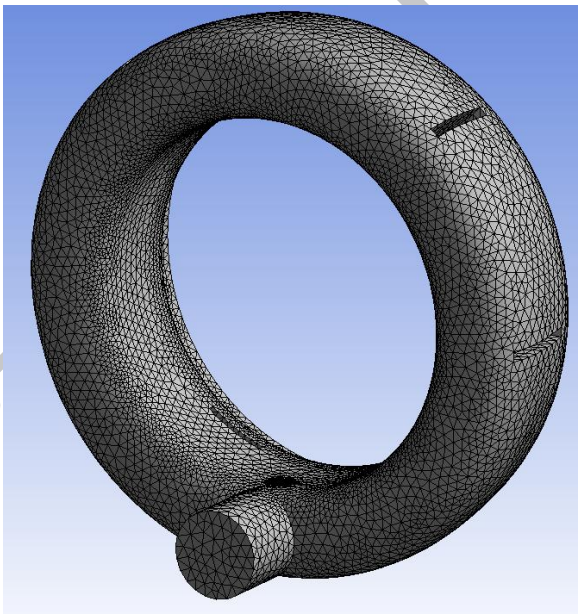

Figure 37 Casing grid with tetrahedron elements

The CFD setup for the nozzle and rotor domains follows the same procedure as explained in section 4.2.2 by only removing the periodic boundary condition as full rotor and nozzle wheels were simulated. As depicted in Figure 38, the casing was considered as an additional stationary component before the nozzle ring with the specification of the inlet boundary conditions (inlet total temperature and pressure) at its inlet instead of the nozzle. Moreover, an extra interface (general grid interface, GGI, connection) was created between the casing outlet and nozzle inlet. CFD setup of the complete RIT stage is illustrated in Figure 38 together with the generated grid for each component. Figure 39 shows the results of

the CFD simulation for the complete RIT stage in terms of the velocity streamlines and performance parameters. It is evident from the velocity streamlines that the level of flow velocity is quite low in the casing (maximum value of about 60m/s compared to the maximum velocity of 238m/s after the nozzle ring) and provided the flow at correct incidence angle around the periphery of the nozzle ring which confirms its acceptable aerodynamic performance according to [23]. Additionally, flow is uniform, preferential and smooth in majority of the nozzle and rotor blade passages without any considerable flow reversals. Although there exists losses in the casing that deteriorated the efficiency and power of the complete RIT stage shown in Figure 39 compared to the results obtained without casing (refer to Figure 31), the variation is in the range of 2.8%, 4.3% and 3.15% for efficiency, power and mass flow rate respectively. Such results show that the CFD model of the complete RIT stage can fairly closely predict the results compared to both nozzle and rotor model as well as the mean-line results. However, with further analysis and optimization of casing geometry such results can be improved.

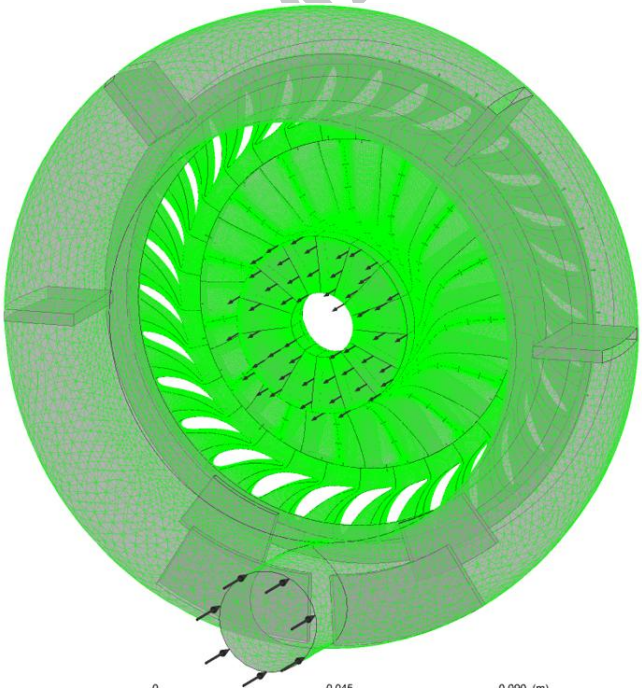

Figure 38 CFD setup of the complete RIT stage with casing

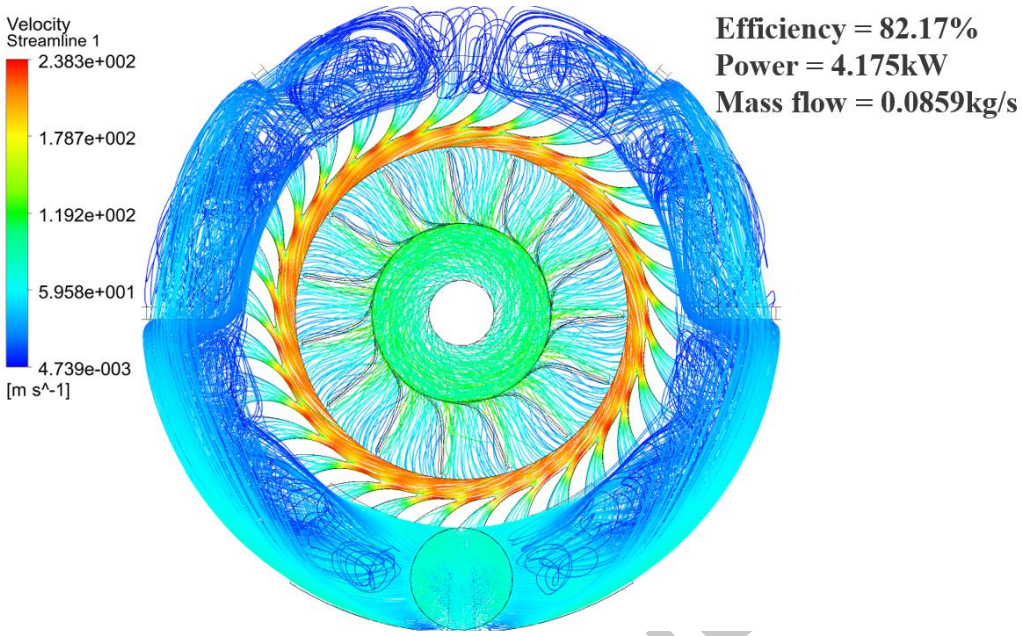

Figure 39 CFD results of complete RIT stage in terms of velocity streamlines and performance parameters

4.3. Finite element analysis (FEA) results

4.3.1. Material selection and properties

In order to carry out the FE analyses, the rotor material needed to be specified. In this study a novel material as Objet FullCure720^{TM} and a pioneering manufacturing method as additive layer manufacturing technique were employed for fabricating the RIT. The potential, effectiveness and advantages of both material and manufacturing method will be highlighted for building functional prototypes in a timely manner as well as reducing manufacturing cost compared to traditional methods (such as 5-axis CNC technique). Objet FullCure720^{TM} is the standard original multi-purpose transparent material widely used in 3-D printers with properties listed in Table 8.

Table 8 Material properties of Objet FullCure 720^{TM}

Parameter	Manufacturer values
Tensile strength (MPa)	60
Modulus of elasticity (MPa)	2870
Flexural strength (MPa)	76
Flexural modulus (MPa)	1718
Density (kg/m^3)	1185
Poisson's ratio (-)	0.27
Glass transition temperature (°C)	50

4.3.2. FEA modelling strategy, grid generation and setup

FE analyses involve investigation of blade stress and displacement under both the fluid pressure on the blade surface and centrifugal forces due to rotational speed. Since the rotor is the critical component amongst all, FEA are merely conducted for this part using ANSYS^{R15} Mechanical. Objet FullCure720^{TM} properties were defined and assigned to the rotor blade. The rotor blade hub surface was specified as a fixed support (Figure 40) for both FEA due to the fluid pressure and due to the rotational speed. For the former, blade surface was selected and the imported pressure from CFD simulation was applied to it. For the latter, rotation axis was defined and design speed of 55000rpm was assigned to it (Figure 40). The aim of all FEA is to ensure that maximum stress and displacement are below the material tensile strength (60MPa) and running clearance (0.56mm between rotor tip and casing) respectively. Therefore, equivalent von-Mises stress and total deformation are defined as the output of FEA.

4.3.3. Mesh sensitivity study and FEA results

Similar to CFD analyses, mesh independence study was carried out using three different grid resolution while the rotor maximum stress and displacement were monitored and results are summarized in Table 9. Tetrahedron mesh type was used to generate grid as demonstrated in Figure 41.

Table 9 Mesh independence study results of FEA

	Number of elements	Maximum von-Mises stress (MPa)		Maximum displacement (mm)	
		Due to pressure	Due to rotation	Due to pressure	Due to rotation
1	4283	0.6309	23.57	0.02055	0.1895
2	14162	0.9819	22.01	0.01615	0.1944
3	50274	1.1104	25.11	0.015	0.1957

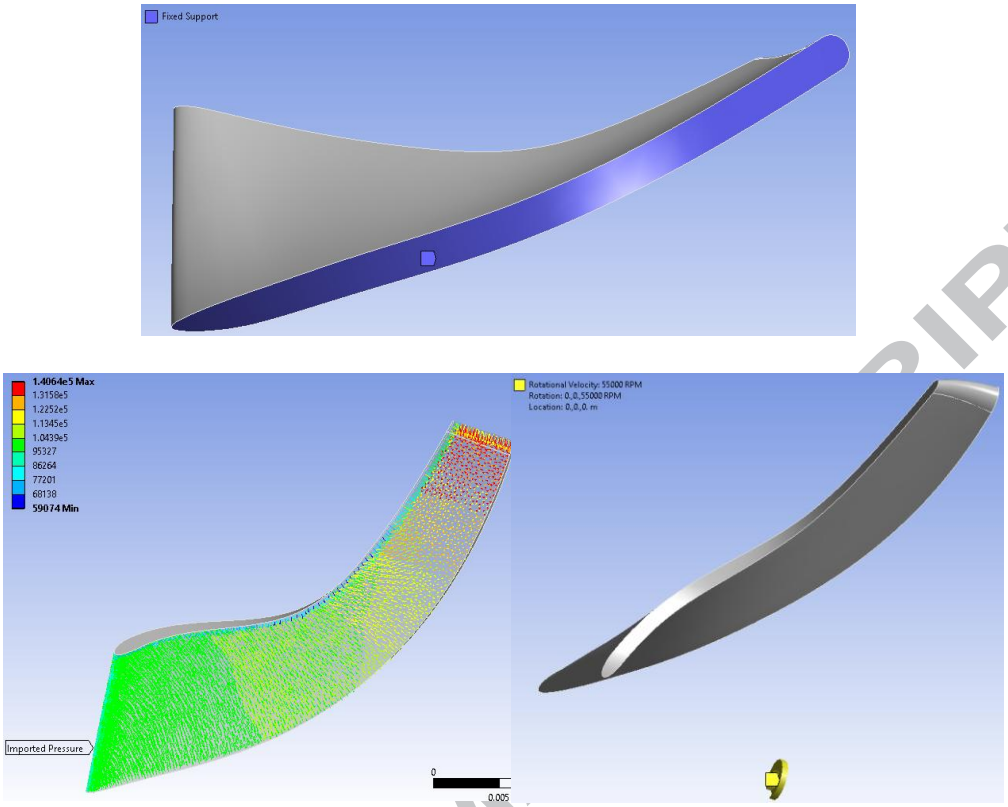

Figure 40 Specified boundary conditions for FEA, (Top) fixed support, (bottom left) imported pressure from CFD, (bottom right) rotational speed and axis of rotation

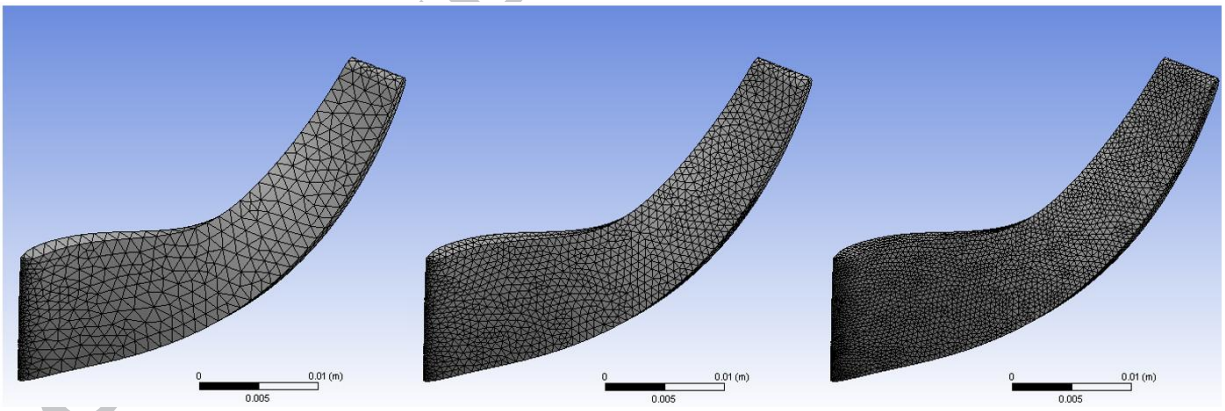

Figure 41 FEA tetrahedron mesh, (left) coarse mesh, (middle) medium mesh, (right) fine mesh

As it is evident from Table 9, there exist considerable deviation between the maximum stress and maximum displacement due to pressure between rows 1 and 2 with the value of 35.7% and 21.41% respectively. However, increasing the number of elements from 14162 to 50274 (rows 2 and 3) reduced such variations to 11.57% and 7% respectively. Additionally, the maximum stress due to the rotational speed increased from 22MPa to 25.11MPa. Therefore, more conservative results from the mesh in row 3 was selected as the grid independence values.

The contour plots for stress and displacement distribution are shown in Figure 42. It is evident that the maximum stress and displacement are all well below the material tensile strength and the running clearance and confirms the mechanical integrity of the developed rotor. The maximum stress occurred in the blade root at hub for both pressure and rotational speed while the maximum displacement was at the blade exit tip for both cases. Therefore, FE analyses were considered sufficient for the purpose of this study.

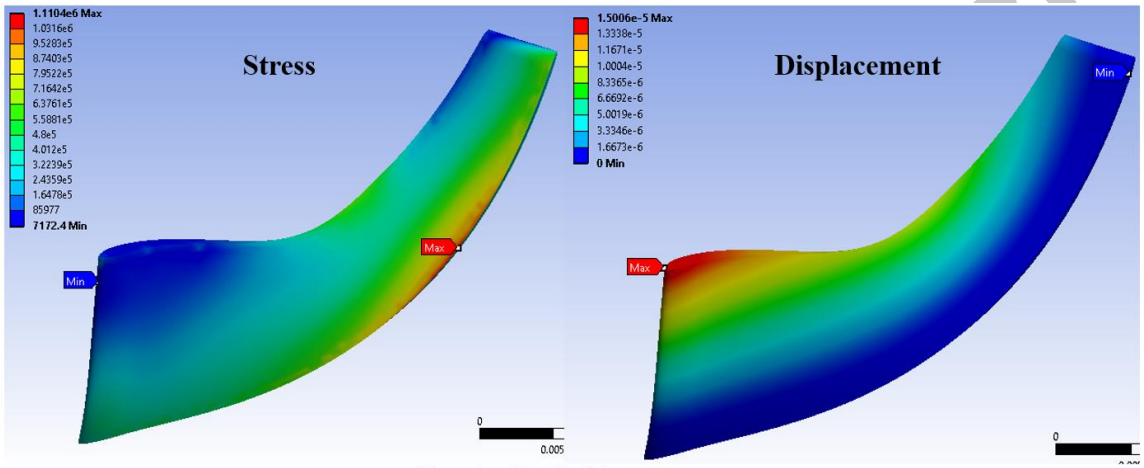

Due to the fluid pressure

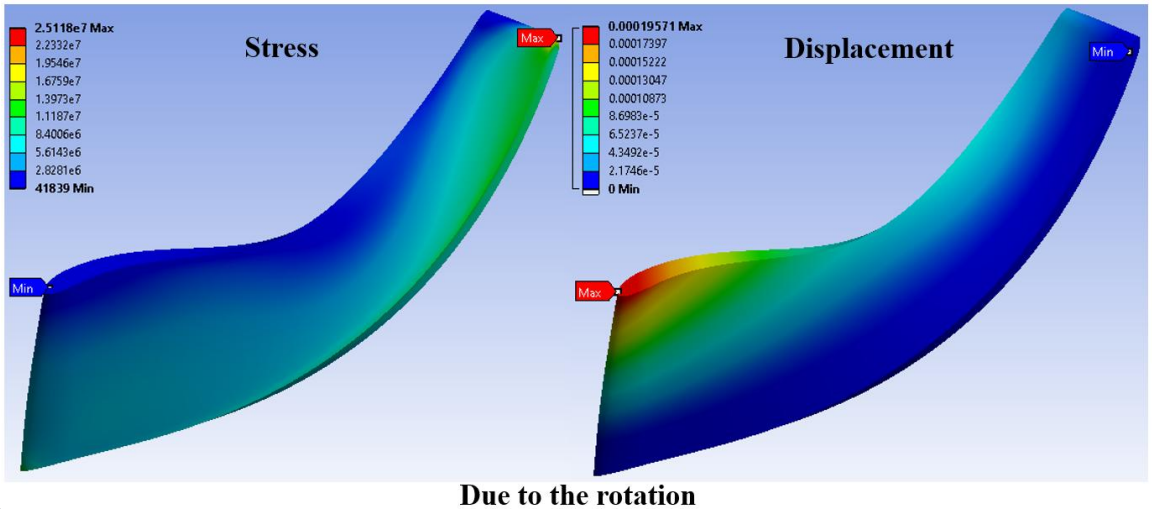

Due to the rotation

Figure 42 Stress and displacement distribution contour plots, (top) due to pressure, (bottom) due to rotation

5. 3-D CAD solid modelling and manufacturing

5.1. CAD modelling

The nozzle ring and rotor wheel together with complementary components as casing, shaft and bearing housing were created using SolidWorks 2014 CAD package. Casing was designed in two pieces to ease its manufacturing (removal of support material). Hybrid ceramic ball bearing was selected to allow for high rotational speed. O-rings and grooves

were accommodated between any two flanges for appropriate sealing. Moreover in the light of earlier FEA (Figure 43), the thickness of casing was determined together with inclusion of stiffening ribs to ensure the mechanical integrity of casing under operating pressure. The CAD model of the complete RIT stage assembly is presented in Figure 44.

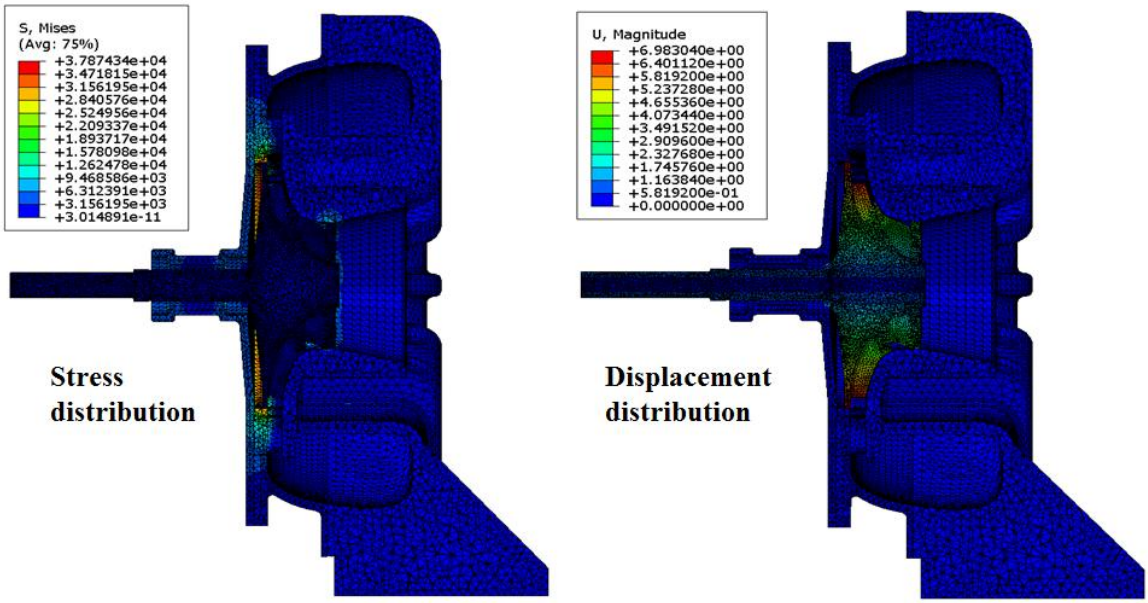

Figure 43 FEA of the complete turbine assembly

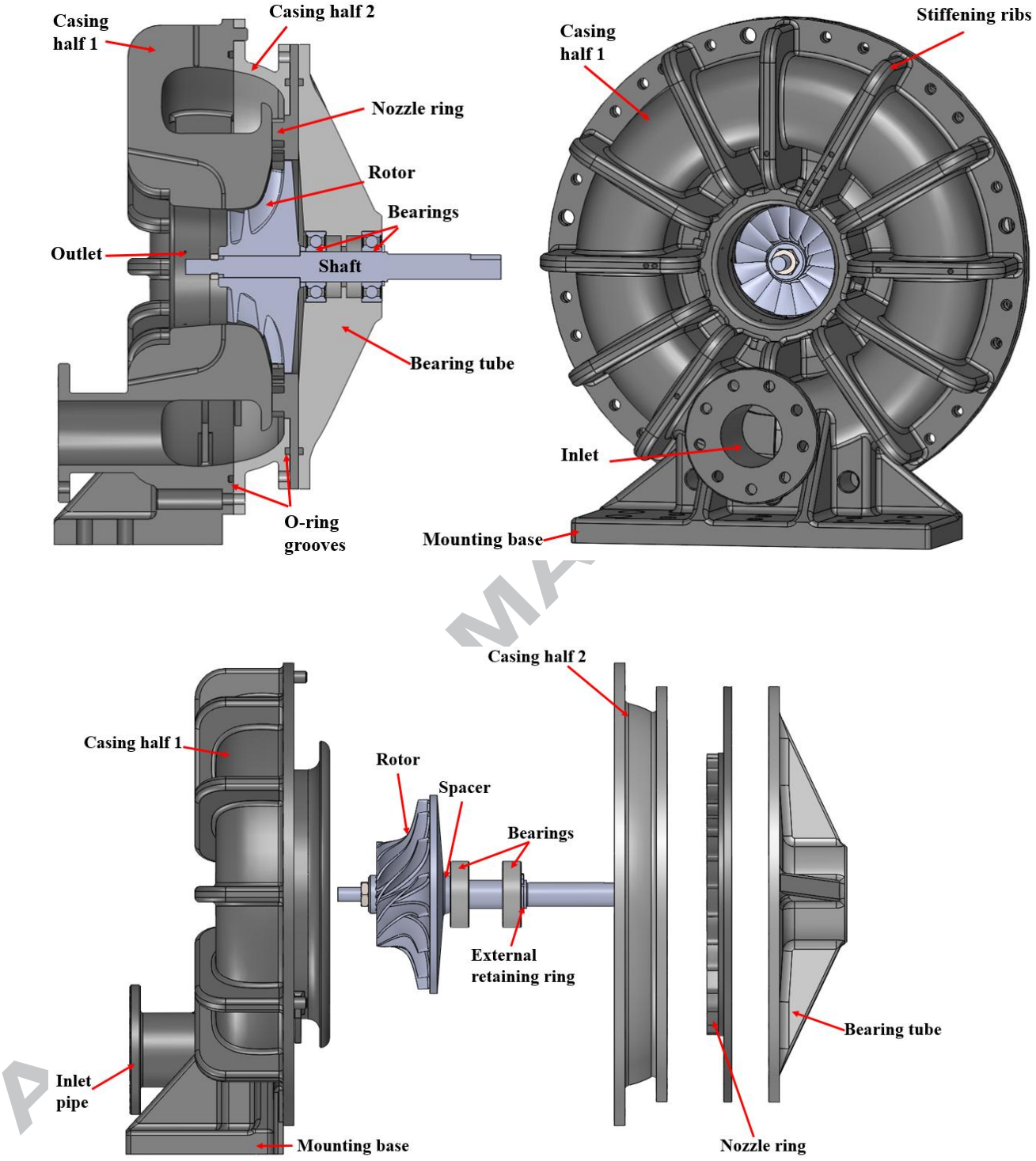

Figure 44 CAD model of the complete RIT stage, (top left) section view, (to right) isometric view, (bottom) exploded view

5.2. Additive layer manufacturing: Stereolithography

Rapid prototyping using additive layer manufacturing technique (3-D printing) is an emerging technology with substantial advancements in the past few years. This technology creates parts layer-by-layer (layer thickness of 32microns) by depositing a

liquid binder onto thin layers of powder. Such procedure is fast, efficient and economical for manufacturing of the parts that are not possible to be manufactured with conventional techniques (i.e. milling and turning) or are substantially expensive. The complete RIT stage were manufactured in-house with the OBJET EDEN 250 3-D printer using objet FullCure 720 at the school of Mechanical Engineering, University of Birmingham. Only the turbine shaft was machined from mild steel. Figure 45 illustrates manufactured parts.

Figure 45 Manufactured turbine components with additive layer manufacturing technique

6. Experimental testing

6.1. Description of experimental facility

Figure 46 presents schematic diagram of the experimental facility for testing of the developed RIT. It consists of a compressed air tank supply, heater tape and control box, flow meter, turbine, instrumentations, torque meter, valves and data acquisition device. The compressed air from the supply tank is initially passed through a filter-regulator to both remove any condensate and dirt from the flow stream and also to regulate the inlet pressure. Regulated air passes through a globe valve to accurately control the flow rate. A section of the piping system is wrapped with a 500W heater tape to enable variation of air temperature at the turbine inlet. The heating rate of heater tape is controlled by a thermocouple at the turbine inlet based on adjusted temperature on the control box. The heated air is then passed through the flow meter to measure flow rate. A pressure gauge is fitted after flow meter and close to turbine inlet to determine pressure. The heated air enters the turbine inlet duct where a Pitot-static tube and thermocouples are fitted for measuring inlet pressure and temperature. Air circulates around the casing, passes through nozzle and rotor and discharges from the turbine exit duct where one pressure transducer and several thermocouples are fitted for measuring the exit pressure and temperature. All the instruments are connected to data loggers which are connected to PC for recording data. The turbine shaft is connected to one end of the torque meter for measuring the rotational speed, torque and power. In order to apply load to the turbine shaft, the other end of torque meter is connected to a brushless DC generator which itself is connected to a variable resistance to facilitate load variation. The data from torque metre is transferred to PC for recording. Figure 47 presents the fabricated test facility and its components.

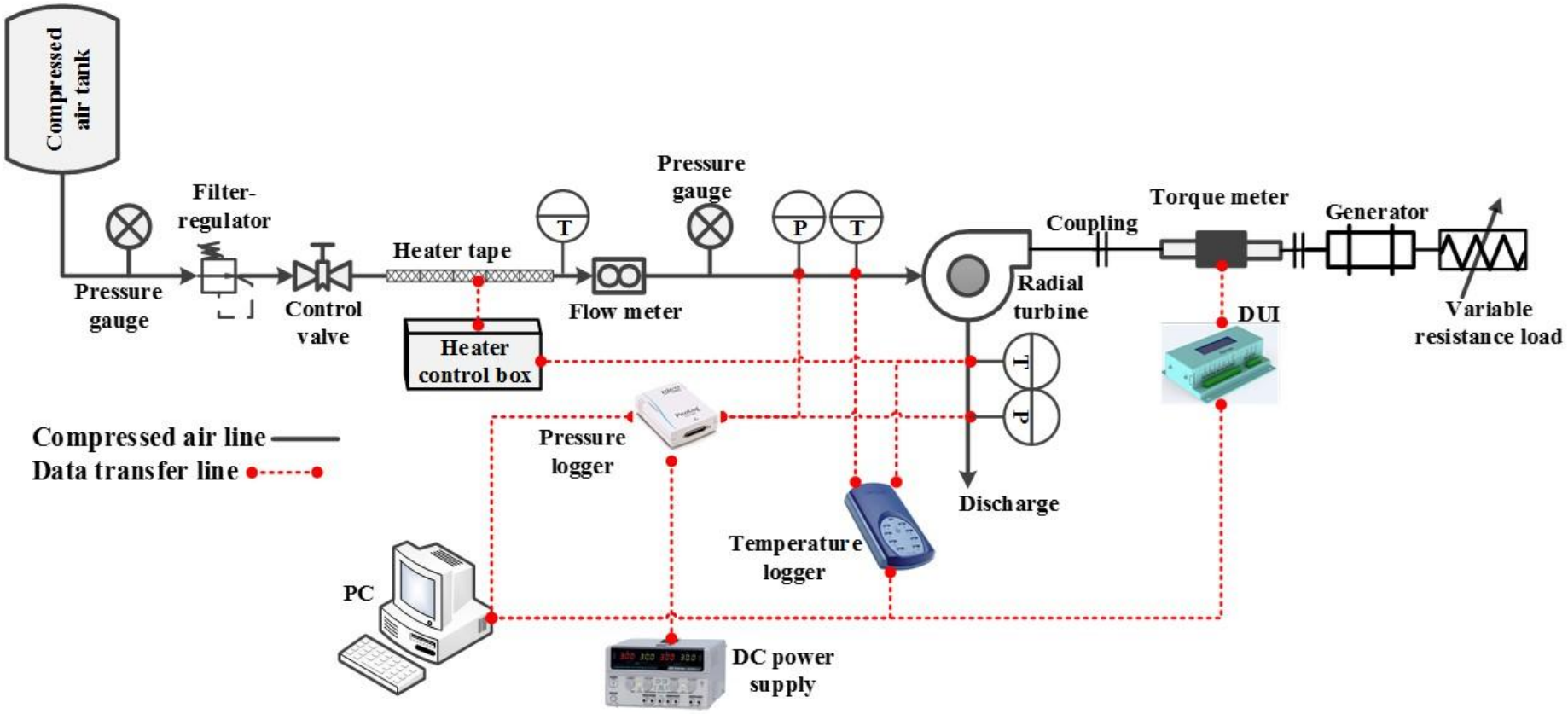

Figure 46 Schematic of the experimental compressed air RIT test facility

Figure 47 Fabricated experimental facility for testing the compressed air RIT

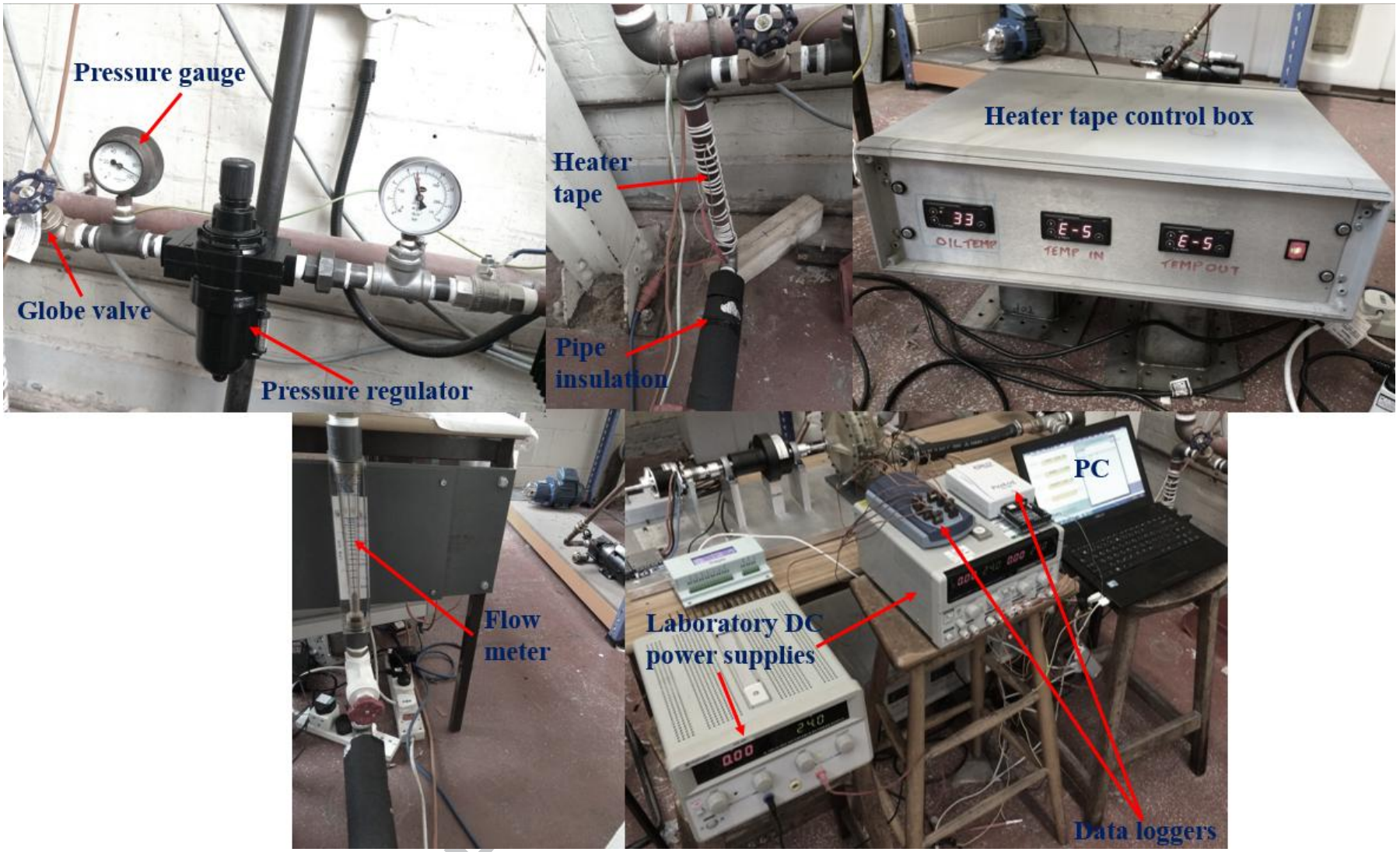

Figure 47 *(Continued)*

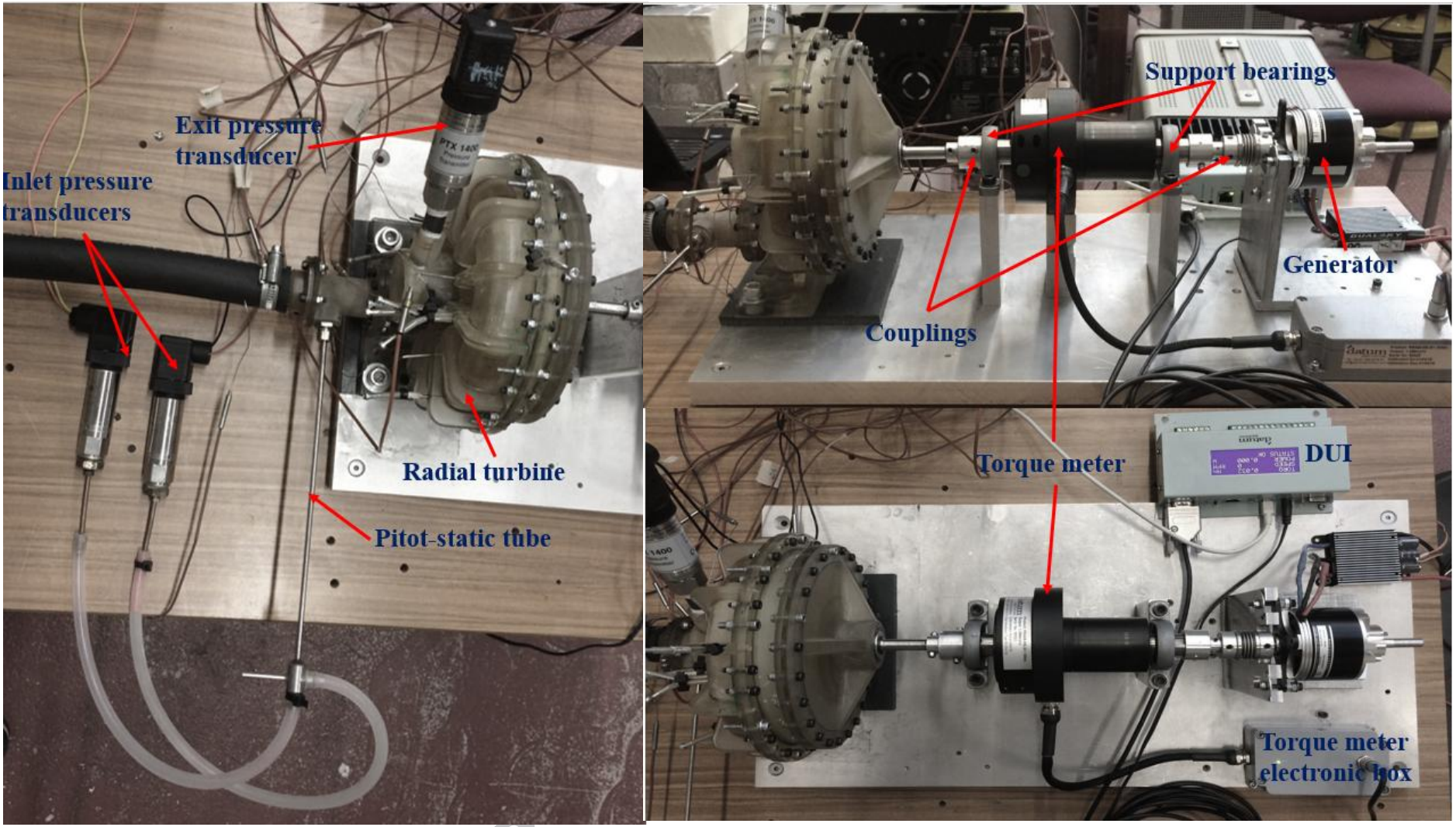

Figure 47 *(Continued)*

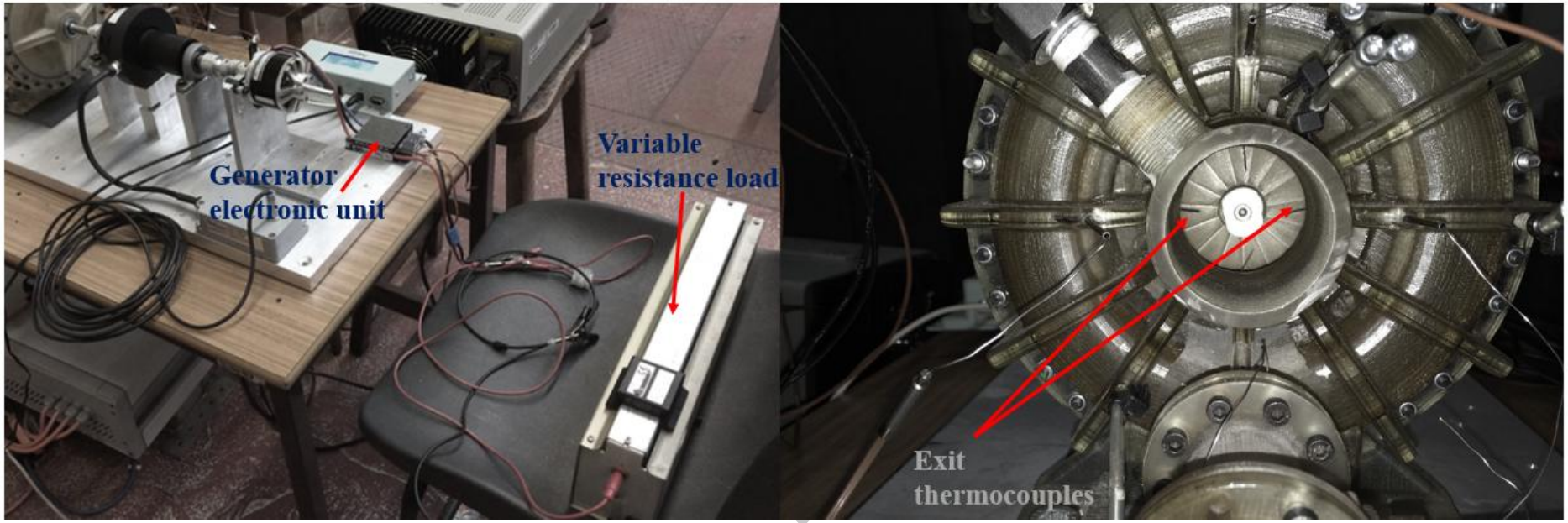

Figure 47 *(Continued)*

6.2. Instrumentation

6.2.1. Thermocouples

Three thermocouples are installed at turbine inlet pipe while four equi-spaced thermocouples are located circumferentially around the turbine exit pipe close to the rotor blade. All thermocouples are T-type Omega TJC100-CPSS-M075G-150 probes with sheath diameter of 0.75mm, length of 150mm and accuracy of ±0.5°C according to the manufacturer. All thermocouples are calibrated against standard PT 100 Platinum Resistance Temperature Detector (RTD) and their calibration formulas are listed in Table 10.

Table 10 Summary of calibration formula and uncertainty of thermocouples

Thermocouple number	Curve fit formula	R^2	Uncertainty (˚C)
Thermocouple-1	1.0101×T-0.7849	0.9999	±0.764
Thermocouple-2	1.0127×T-0.9378	1	±0.712
Thermocouple-3	1.0124×T-0.8724	1	±0.697
Thermocouple-4	1.0121×T-0.2993	1	±0.653
Thermocouple-5	1.01×T-0.3848	0.9999	±0.607
Thermocouple-6	1.0105×T+0.2354	0.9999	±0.735
Thermocouple-7	1.0148×T-0.3227	1	±0.726

6.2.2. Pitot-static tube and pressure transducers

Turbine inlet pipe is instrumented with a Pitot-static tube to measure total and static pressures simultaneously. Each of the Pitot tube ports is connected to 10bar GE UNIK 5000 pressure transducers directly. A 6bar Druck PTX 1400 pressure transducer is fitted at the turbine exit duct for measuring exit static pressure. All pressure transducers are 4-20 mA current output with accuracy of ±0.04% full scale according to the manufacturer. 100 ohms resistances are connected to data logger external terminal board to convert the current signal to voltage signal (up to 2 volt). The pressure transducers are excited with 0.005A and 24V from a ISO-TECH IPS4303 laboratory DC power supply. Pressure transducers are calibrated against a certified pressure gauge (with accuracy of ±0.0397bars) in pressurized water cylinder (Water Dead-Weight Testers) and their calibration formulas are listed in Table 11.

Table 11 Summary of the calibration formula and uncertainty of pressure transducers

Transducer	Curve fit formula	R^2	Uncertainty (Bar)
GE UNIK 5000-1	6.324× volt-2.5024	0.9999	±0.0421
GE UNIK 5000-2	6.3001× volt-2.4748	0.9999	±0.0416
Druck PTX 1400	3.7506× volt -1.4925	0.9999	±0.0414

6.2.3. Flow meter

A variable area (Rotameter) series FR5000I-5A55 acrylic air flow meter manufactured by KEY instruments Ltd is used ranging from 400 to 4000litre/min and with accuracy of ±2% full scale according to the manufacturer.

6.2.4. Torque transducer

A contactless rotary torque transducer series RS425-S1-HS was built by Datum electronics Ltd according to the specifications of torque range (0-10Nm), rotational speed (max 20,000rpm) and samples per second (100) to measure the turbine's torque, power and speed. Such configuration is advantageous as it is not limited by speeds found in the traditional inline torque transducers and has no wear and tear on the transducer. The torque transducer was factory-calibrated and certified with the accuracy of ±0.1% full scale according to the certification. The torque transducer was paired up with the datum universal interface (DUI) to give a complete range of outputs (connected to PC).

6.2.5. Data acquisition

All thermocouples are connected directly to a Pico TC-08 data logger and pressure transducers are connected to a Pico 1012 general purpose and both connected to PC. Torque transducer is directly connected to DUI which is connected to PC for recording torque, speed, and power.

7. Experimental results and validation of CFD model

The experiments are conducted for a range of turbine inlet temperature, pressure, flow rate and rotational speed. Initially, turbine inlet temperature is adjusted using the control box to control the heat flux from the heater tape. For each set of experiments the turbine inlet temperature was fixed while varying other above-mentioned parameters. Then the turbine inlet pressure is varied using the pressure regulator to create a series of off-design points at various

speeds and mass flow rates. Apparently, as the turbine inlet pressure is increased the turbine rotational speed is also escalated. Therefore to fix the turbine rotational speed, load on the DC generator is adjusted using the variable resistance while increasing the turbine inlet pressure. Obviously, the higher the turbine inlet pressure the larger the required load on the turbine shaft. The recorded temperatures at the turbine inlet and exit are averaged to obtain a single value for each operating point. Then for each experimental point, the recorded measurements are used for calculation of efficiency and power as following.

$$\eta_{stage,ts} = \frac{1 - \frac{T_{t,5}}{T_{t,4}}}{1 - (\frac{P_5}{P_{t,4}})^{\frac{\gamma-1}{\gamma}}} \quad \text{Equation 57}$$

$$Power = \tau\omega \quad \text{Equation 58}$$

Where τ is the torque (Nm) produced by the turbine and recorded by the torque meter and ω is the rotational speed (rad/s). Although the employed torque meter is amongst the highest speed transducers in the market, it was unable to be spun more than 20000rpm (based on the manufacturer). Therefore, it was not possible to run the turbine up to its design speed of 55000rpm and the test facility was used to obtain the turbine performance under off-design operating conditions. The experiments were conducted at five different levels of turbine rotational speed as 4000rpm, 8000rpm, 12000rpm, 16000rpm and 20000rpm while the turbine inlet temperature was varied from 20°C to 40°C at steps of 5°C and results are shown in Figures 48 to 52. As evident from results, for each experimental data point the error bars are also included. Such errors were obtained by including uncertainty of the measuring devices and calculated using EES software. Simultaneously, the CFD model of RIT assembly (casing, full nozzle ring and full rotor wheel) developed in section 4.2.7 was employed to validate the accuracy of CFD simulations. The same turbulence model, convergence criteria and boundary conditions were applied to the model. The measured turbine inlet total pressure and temperature were specified at the casing inlet while measured static pressure was specified at rotor exit and the measured rotational speed was specified to the rotor wheel. The CFD simulations were conducted for all experimental data points as shown in Figures 48 to 52.

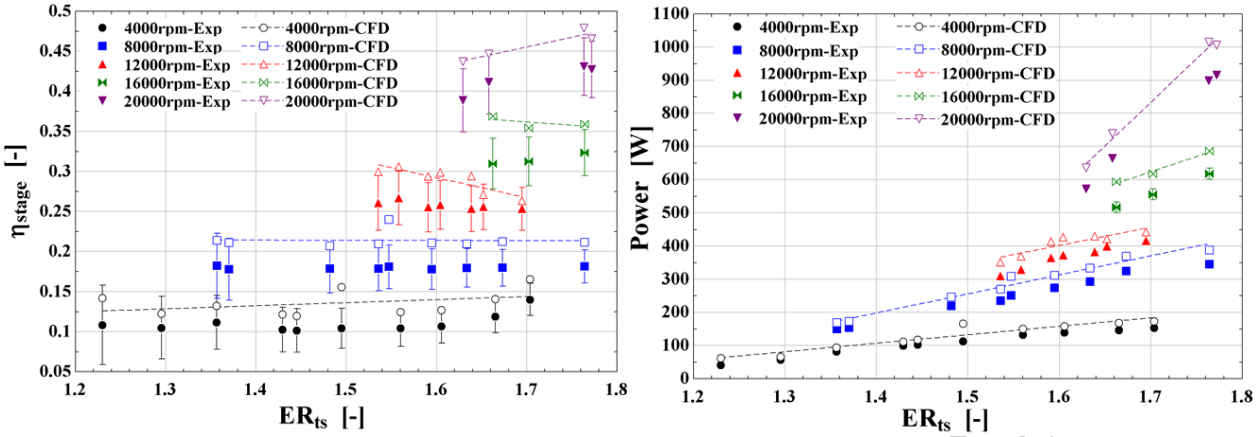

Figure 48 Validation of CFD model with experimental results (power and efficiency) for the turbine inlet temperature of 20°C

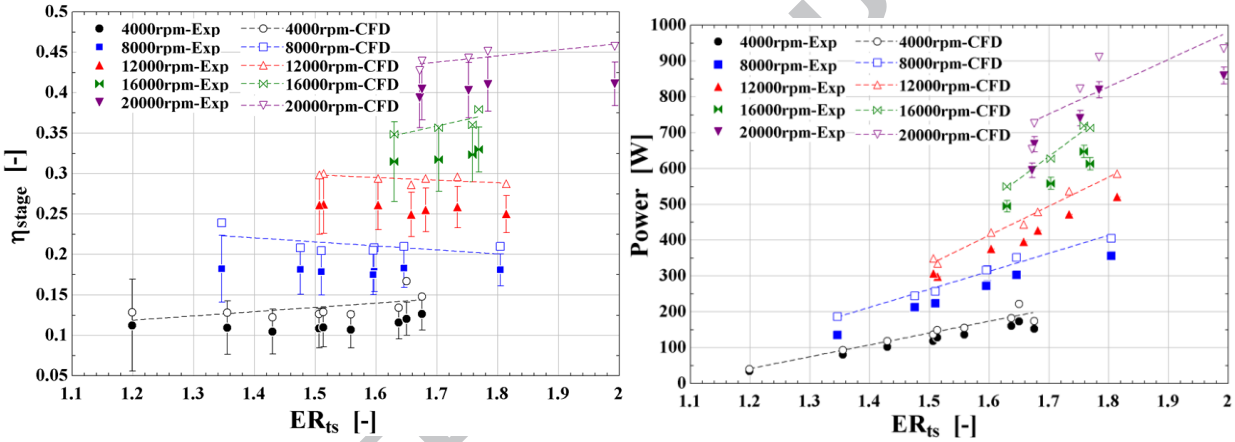

Figure 49 Validation of CFD model with experimental results (power and efficiency) for the turbine inlet temperature of 25°C

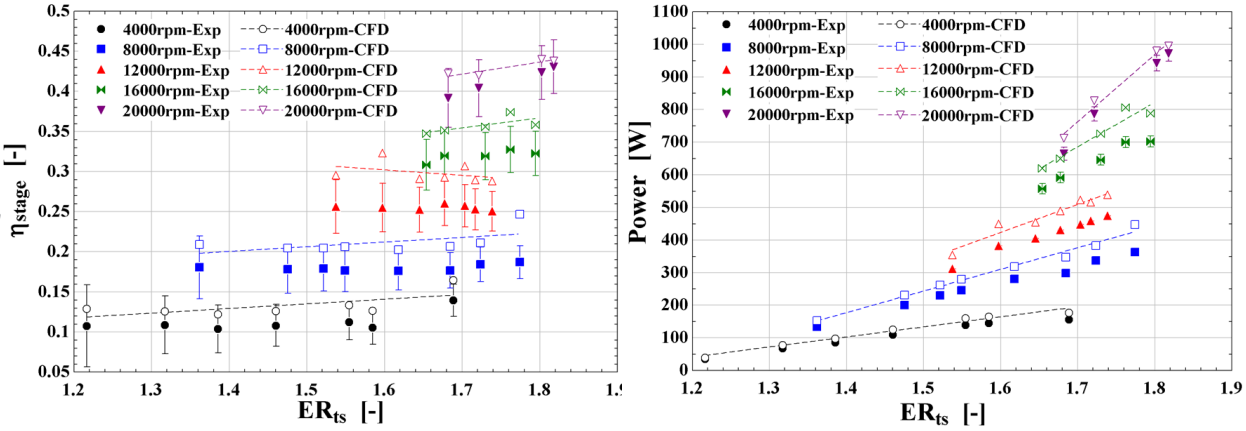

Figure 50 Validation of CFD model with experimental results (power and efficiency) for the turbine inlet temperature of 30°C

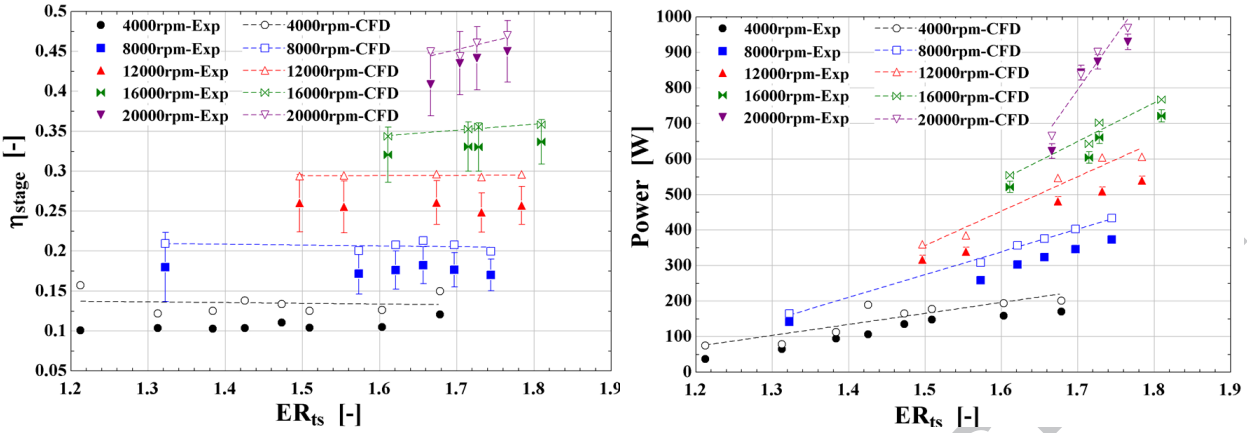

Figure 51 Validation of CFD model with experimental results (power and efficiency) for the turbine inlet temperature of 35°C

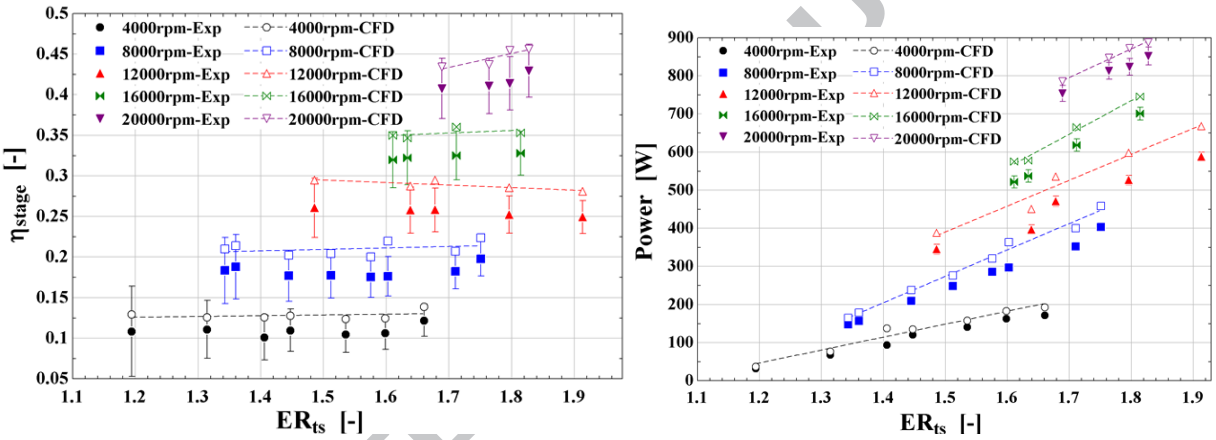

Figure 52 Validation of CFD model with experimental results (power and efficiency) for the turbine inlet temperature of 40°C

As it is evident from the results, the turbine efficiency is more affected by the rotational speed while the turbine power output is considerably affected by both the turbine expansion ratio as well as the rotational speed. Moreover, in all of the investigated data points, the CFD simulations were over-predicting the power and efficiency due to the following factors:

I. Surface roughness of the manufactured turbine blade compared to smooth blade assumption in CFD simulations.

II. Exclusion of rotor back plate flow leakage (windage loss) in CFD compared to actual experimental conditions.

III. Mechanical losses in bearings which reduced the power output of experimental results compared to CFD.

IV. Manufacturing tolerances in terms of the nozzle throat area of the fabricated part compared to the designed one (probably smaller throat opening in the manufactured nozzle compared to designed one).

To effectively compare the accuracy of developed CFD model, all the experimental data and CFD simulations are plotted in one graph for both power and efficiency as shown in Figures 53 and 54 with boundary error lines are obtained from Equation 59.

$$Error\ (\%) = \frac{|Experimental - CFD|}{CFD} \times 100 \qquad \text{Equation 59}$$

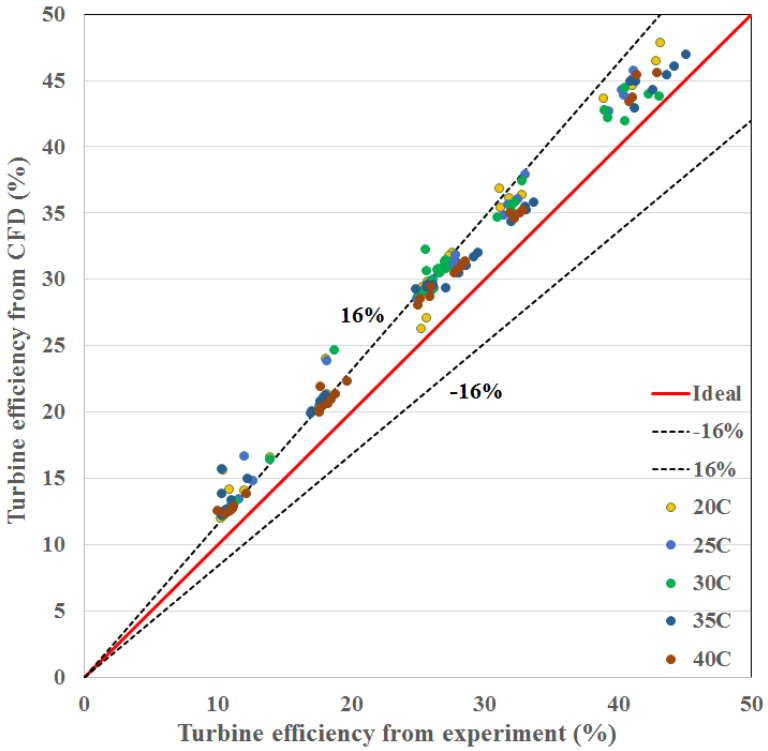

Figure 53 Comparison of efficiency from CFD simulations with experiments for all data points

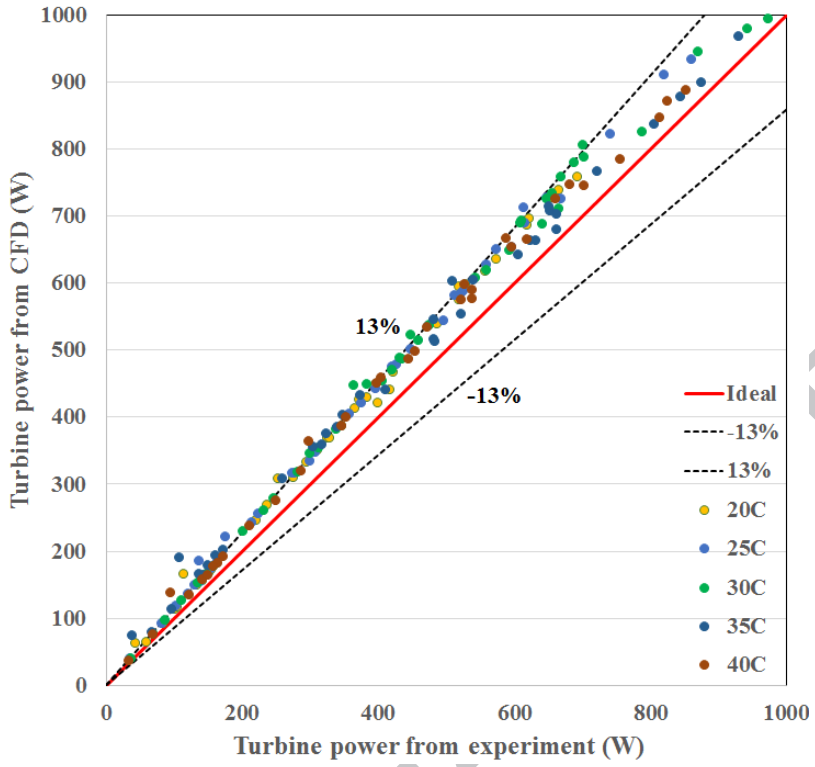

Figure 54 Comparison of power from CFD simulations with experiments for all data points

The CFD predictions of the turbine efficiency for majority of experimental data were in the range of ±16% of the ideal line as depicted in Figure 53 while the CFD predictions of the turbine power for majority of experimental data were in the range of ±13% as presented in Figure 54. Such results show that the developed CFD model can fairly accurately predict the performance of the developed RIT stage and the proposed modelling strategy can be used as a benchmarking model for developing small-scale RITs for various applications such as the CAES and ORC.

8. Conclusions

There is a need for developing efficient expanders for CAES and ORC that can provide energy demands through DPG systems. This study proposed a systematic methodology for developing small-scale RIT for such applications that allows improving turbine performance using both simple and complex numerical tools as well as manufacturing and experimental testing for validation purposes. A novel code was developed for 1-D modelling that enables fairly accurate estimation of the turbine performance as well as obtaining the key geometrical

parameters of the RIT stage in a timely manner by variation of turbine input design variables. Although such approach is fast, due to the complex nature of the flow field in RIT, CFD analysis were conducted to breakdown the flow field in greater details as well as improving turbine geometry for better performance. The shape of rotor blade in terms of blade angle and thickness distributions and number of rotor blades was modified and turbine efficiency was improved from 81.3% obtained by mean-line modelling to 84.5% obtained by CFD. Such results highlights the advantages of the CFD parametric studies, though, each of these steps were vital for reaching to the optimum turbine geometry. Without proper 1-D modelling, long time might be spent making trial CFD analyses that were far from the optimum. FEA analysis ensured mechanical integrity of turbine rotor blade in terms of maximum stress and displacement. Experimental results showed that the turbine efficiency was more sensitive to ω while turbine power was sensitive to both ER_{ts} and ω. The developed CFD model of RIT stage was validated and it was shown that CFD model can predict the turbine efficiency with accuracy of $\pm$16% while the turbine power was predicted with accuracy of $\pm$13%. Results underlined the effectiveness of the proposed methodology and demonstrated that the CFD model can fairly accurately predict the turbine performance over a wide range of operating conditions. Such model can be used as benchmarking model for analyses of small-scale RITs with reasonable accuracy and for various applications such as CAES and ORC systems. Additionally, the novel manufacturing technique and pioneering material enables to build functional prototypes quick and economical which are suitable for laboratory tests, performance validation and design decisions.

Nomenclature

Symbols

A	Area (m^2)
b	Blade height (m)
BK	Blockage factor (-)
C	Absolute flow velocity (m/s)
C_{nozzle}	Nozzle chord length (m)
C_p	Specific heat capacity at constant pressure (J/kg-K)
C_s	Spouting velocity $(J/kg)^{-1}$
d	Diameter (m)
d_{hyd}	Hydraulic diameter (m)
ER	Expansion ratio (-)
f	Friction coefficient (-)
f_{curve}	Turbine friction factor (-)

h	Enthalpy (J/kg)
Δh_{actual}	Actual specific enthalpy drop (J/kg)
Δh_{ideal}	Ideal specific enthalpy drop (J/kg)
Δh_{losses}	Enthalpy drop due to losses (J/kg)
I	Rothalpy (J/kg)
k	Coefficient (-)
l	Length (m)
l_{hyd}	Hydraulic length (m)
$\dot{m}$	Mass flow rate (kg/s)
Ma	Mach number (-)
N_s	Specific speed (-)
$O_{throat,nozzle}$	Nozzle throat width (m)
P	Pressure (Pa)
R	Gas constant (J/kg-K)
R_0	Universal gas constant ((J/(k.mol))
RR	Relative roughness (m)
Re	Reynolds number (-)
r	Radius (m)
$\boldsymbol{r}$	Location vector (m)
r_c	Mean radius of curvature (m)
S	Entropy (J/kg-K)
$\boldsymbol{S}_E$	Energy source (kg/(m.s^3))
$\boldsymbol{S}_M$	Momentum source ((kg/(m^2-s^2))
S_{nozzle}	Nozzle blade pitch (m)
T	Temperature (K)
t	time (s)
U	Rotor blade velocity (m/s)
$\boldsymbol{U}$	Vector velocity $\boldsymbol{U}_{x,y,z}$ (m/s)
W	Relative flow velocity (m/s)
w	Molecular weight (kg/mol)
Z	Blade number (-)
Greek letters	
α	Absolute flow angle with respect to radial (degree)
β	Relative flow angle with respect to radial (degree)
γ	Specific heat capacity ratio (-)
δ	Identity matrix (-)
ε	Clearance (m)
ζ	Shear stress tensor (kg/m-s^2)
η	Efficiency (-)
λ	Thermal conductivity (W/m.K)
μ	Dynamic viscosity (kg/(m-s))
υ	Isentropic velocity ratio (-)
ρ	Density (kg/m^3)
σ	Solidity (-)
φ	Flow coefficient (-)
ψ	Loading coefficient (-)

ω	Rotational velocity (RPM)
Subscripts	
1-5	Stations across turbine
abs	Absolute
b	Back plate
cfg	Centrifugal
Cor	Coriolis
f	Friction
hub	Rotor hub
j	Counter
m	Meridional direction
r	Radial
ref	Reference
rel	Relative
rms	Root mean square
rotor	Rotor
s	Isentropic
sonic	Sonic velocity (speed of sound)
x	Axial direction
stage	Turbine inlet to turbine outlet
stat	Static
t	Total, stagnation
tip	Rotor tip
ts	Total to static
θ	Tangential direction
Superscripts	
T	Matrix transpose
‾	Average
Mathematical operators	
∇	Vector operator $\left[\frac{\partial}{\partial x}, \frac{\partial}{\partial y}, \frac{\partial}{\partial z}\right]$
$\otimes$	Dyadic operator (tensor product)
Acronyms	
CAES	Compressed air energy storage
CAD	Computer aided design
CFD	Computational fluid dynamics
CHP	Combined heat and power
CPG	Centralized power generation
DPG	Distributed power generation
DUI	Datum universal interface
EES	Engineering equation solver
FEA	Finite element analysis
GGI	General grid interface,
IEA	International energy agency
LE	Leading edge
MOGA	Multi-objective genetic algorithm

ORC	Organic Rankine cycle
PS	Pressure surface
RANS	Reynolds-averaged Navier-Stokes
RIT	Radial inflow turbine
RPM	Revolutions per minute
SS	Suction surface
SST	Shear stress transport
TE	Trailing edge

References

1. International Energy Agency, I., *Energy Technology Perspectives–ETP2014, Harnessing electricity's potential* 2014.
2. World Energy Council *World Energy Perspective- Energy Efficiency Technologies*, 2013.
3. Ackermann, T., G. Andersson, and L. Söder, *Distributed generation: a definition.* Electric Power Systems Research, 2001. **57**(3): p. 195-204.
4. Safaei, H., D.W. Keith, and R.J. Hugo, *Compressed air energy storage (CAES) with compressors distributed at heat loads to enable waste heat utilization.* Applied Energy, 2013. **103**: p. 165-179.
5. Kokaew, V., M. Moshrefi-Torbati, and S.M. Sharkh, *Maximum Efficiency or Power Tracking of Stand-alone Small Scale Compressed Air Energy Storage System.* Energy Procedia, 2013. **42**: p. 387-396.
6. Lemofouet, S. and A. Rufer, *A Hybrid Energy Storage System Based on Compressed Air and Supercapacitors With Maximum Efficiency Point Tracking (MEPT).* Industrial Electronics, IEEE Transactions on, 2006. **53**(4): p. 1105-1115.
7. Briola, S., P. Di Marco, R. Gabbrielli, and J. Riccardi, *A novel mathematical model for the performance assessment of diabatic compressed air energy storage systems including the turbomachinery characteristic curves.* Applied Energy, 2016. **178**: p. 758-772.
8. Zhao, P., L. Gao, J. Wang, and Y. Dai, *Energy efficiency analysis and off-design analysis of two different discharge modes for compressed air energy storage system using axial turbines.* Renewable Energy, 2016. **85**: p. 1164-1177.
9. Maia, T.A.C., J.E.M. Barros, B.J. Cardoso Filho, and M.P. Porto, *Experimental performance of a low cost micro-CAES generation system.* Applied Energy, 2016. **182**: p. 358-364.
10. Ennil, A.B., R. Al-Dadah, S. Mahmoud, K. Rahbar, and A. AlJubori, *Minimization of loss in small scale axial air turbine using CFD modeling and evolutionary algorithm optimization.* Applied Thermal Engineering, 2016. **102**: p. 841-848.
11. Yao, E., H. Wang, L. Wang, G. Xi, and F. Maréchal, *Thermo-economic optimization of a combined cooling, heating and power system based on small-scale compressed air energy storage.* Energy Conversion and Management, 2016. **118**: p. 377-386.
12. Bao, J. and L. Zhao, *A review of working fluid and expander selections for organic Rankine cycle.* Renewable and Sustainable Energy Reviews, 2013. **24**(0): p. 325-342.
13. Martins, G.L., S.L. Braga, and S.B. Ferreira, *Design optimization of partial admission axial turbine for ORC service.* Applied Thermal Engineering, 2016. **96**: p. 18-25.
14. Manente, G., L. Da Lio, and A. Lazzaretto, *Influence of axial turbine efficiency maps on the performance of subcritical and supercritical Organic Rankine Cycle systems.* Energy, 2016. **107**: p. 761-772.
15. Rahbar, K., S. Mahmoud, and R. Al-Dadah. *Optimized efficiency maps and new correlation for performance prediction of ORC based on radial turbine for small-scale applications*. in *3rd*

International Seminar on ORC Power Systems. 12-14 October, 2015. Brussels, Belgium: ASME ORC.

16. Rahbar, K., S. Mahmoud, R.k. Al-Dadah, and N. Moazami, *Parametric analysis and optimization of a small-scale radial turbine for Organic Rankine Cycle.* Energy, 2015 [a]. **83**(0): p. 696-711.
17. Rahbar, K., S. Mahmoud, R.K. Al-Dadah, and N. Moazami, *Modelling and optimization of organic Rankine cycle based on a small-scale radial inflow turbine.* Energy Conversion and Management, 2015 [b]. **91**(0): p. 186-198.
18. Rahbar, K., S. Mahmoud, R.K. Al-Dadah, and N. Moazami. *Integrated Modelling and Multi-Objective Optimization of Organic Rankine Cycle Based on Radial Inflow Turbine,GT2015-42835*. in *ASME Turbo Expo 2015: Turbine Technical Conference and Exposition*. June 15–19, 2015. Montreal, Quebec, Canada.
19. Moustapha, H., M. Zelesky, N. Baines, and D. Japikse, *Axial and radial turbines*. 1st ed ed. 2003, White River Junction, VT: Concepts NREC.
20. Rahbar, K., S. Mahmoud, and R. Al-Dadah, *Mean-line modeling and CFD analysis of a miniature radial turbine for distributed power generation systems.* International Journal of Low-Carbon Technologies:doi: 10.1093/ijlct/ctu028, 2014.
21. Whitfield, A. and N.C. Baines, *Design of radial turbomachines*. 1990, Harlow, Essex, England; New York, NY: Longman Scientific & Technical ; Wiley.
22. Klein, S. *Engineering equation solver: F-chart Software* 2013.
23. Baines, N., *Part 3: Radial Turbine Design*, in *Axial and Radial Turbines*. 2003, Concepts NREC: VT. p. pp. 197-326.
24. Aungier, R.H., *Turbine aerodynamics : axial-flow and radial-inflow turbine design and analysis*. 2006, New York: ASME Press.
25. Glassman, A.J. and C. Lewis Research, *Computer program for design analysis of radial-inflow turbines*. NASA technical note ;NASA TN D-8164. 1976, Washington, D.C. : [Springfield, Va.: National Aeronautics and Space Administration ; For sale by the National Technical Information Service]. 64 p.
26. Benson, R., *A Review of Methods for Assessing Loss Coefficients in Radial Gas Turbines.* International Journal of Mechanical Sciences, 1970. **12**(10): p. 905-932.
27. Watanabe, I., I. Ariga, and T. Mashimo, *Effect of Dimensional Parameters of Impellers on Performance Characteristics of a Radial-Inflow Turbine.* Journal of Engineering for Gas Turbines and Power, 1971. **93**(1): p. 81-102.
28. Suhrmann, J., D. Peitsch, M. Gugau, T. Heuer, and U. Tomm. *Validation and development of loss models for small size radial turbines.* in *Proceedings of ASME Turbo Expo : Power for land, sea and Air GT2010*. 2010. Glasgow, UK.
29. Musgrave, D. *The Prediction of Design and Off-Design Efficiency for Centrifugal*

Compressor Impellers. in *Twenty-Fifth Annual International Gas Turbine Conference and Exhibit and Twenty-Second Annual Fluids Engineering Conference*. 1980. New Orleans, Louisiana, USA: ASME.

30. Churchill, S., *Friction-factor equation spans all fluid-flow regimes.* Chemical Engineering, 1977. **84**: p. 91–92.
31. Rodgers, C. and R. Geiser, *Performance of a High-Efficiency Radial/Axial Turbine.* Journal of Turbomachinery, 1987. **109**(2): p. 151-154.
32. K. Rahbar, S. Mahmoud, R. K. Al-Dadah, and N. Moazami, *One-Dimensional and Three-Dimensional Numerical Optimization and Comparison of Single-Stage Supersonic and Dual-Stage Transonic Radial Inflow Turbines for the ORC*, in *ASME 2016 Power Conference*2016, ASME Charlotte, North Carolina, USA,. p. V001T08A017; 15 pages.

33. Menter, F.R., *Two-equation eddy-viscosity turbulence models for engineering applications.* AIAA Journal, 1994. **32**(8): p. 1598-1605.
34. de Souza, R. and G. Filho, *Automotive Turbocharger Radial Turbine CFD and Comparison to Gas Stand Data.* SAE Technical Paper 2005-01-1171, 2011.

Highlights

- Proposing methodology for developing small-scale RIT as expander of CAES and ORC
- 1D modelling enables estimation of turbine performance and obtaining key geometry
- Turbine efficiency improved from 81.3% obtained by 1D model to 84.5% obtained by CFD
- CFD predicts turbine efficiency and power with accuracy of $\pm$16% and $\pm$13% compared to tests